RESEARCH ARTICLE SUMMARY

METABOLISM

Dietary pro-oxidant therapy by a vitamin K precursor targets PI 3-kinase VPS34 function

Manojit M. Swamynathan, Shan Kuang†, Kaitlin E. Watrud†, Mary R. Doherty†, Charlotte Gineste, Grinu Mathew, Grace Q. Gong, Hilary Cox, Eileen Cheng, David Reiss, Jude Kendall, Diya Ghosh, Colleen R. Reczek, Xiang Zhao, Tali Herzka, Saulė Špokaitė, Antoine N. Dessus, Seung Tea Kim, Olaf Klingbeil, Juan Liu, Dawid G. Nowak, Habeeb Alsudani, Tse-Luen Wee, Youngkyu Park, Francesca Minicozzi, Keith Rivera, Ana S. Almeida, Kenneth Chang, Ram P. Chakrabarty, John E. Wilkinson, Phyllis A. Gimotty, Sarah D. Diermeier, Mikala Egeblad, Christopher R. Vakoc, Jason W. Locasale, Navdeep S. Chandel, Tobias Janowitz, James B. Hicks, Michael Wigler, Darryl J. Pappin, Roger L. Williams, Paolo Cifani, David A. Tuveson, Jocelyn Laporte, Lloyd C. Trotman*

INTRODUCTION: Prostate cancer (PC) is the most commonly diagnosed cancer in men, with more than 299,000 new cases anticipated in the United States in 2024. The majority of these men will present with slow-growing disease that can turn into life-threatening PC that resists all available treatment options. Therefore, there is a strong interest in defining well-informed lifestyle, dietary, and supplement choices that can slow down disease progression. This has spawned large-scale human trials, including one on the benefits of dietary antioxidants: The SELECT trial (Selenium and Vitamin E Cancer Prevention Trial) followed 35,533 healthy men for more than 10 years. Against expectations, SELECT showed significantly increased risk of developing PC among men who took the antioxidant vitamin E supplements.

RATIONALE: The PC-promoting effect of antioxidant vitamin E supplements immediately raised the question whether, conversely, pro-oxidant supplements can help prevent the disease. Genetically engineered mouse (GEM) models of PC provide a platform to ask this question. Specifically, we use the RapidCaP GEM model, which allowed us to determine whether and how fast a cancer in the prostate progresses to the metastatic form.

RESULTS: We treated RapidCaP animals with the pro-oxidant menadione supplement [menadione sodium bisulfite (MSB)], a precursor of mammalian vitamin K that is present in circulation after consumption of plant vitamin K from greens. Daily MSB supplementation in drinking water suppressed PC progression, yielding durable responses. Systematic analysis of cell d pathways revealed that MSB kills cancer through a distinct oxidative cell death mechanism that we propose to call triaptosis. We used genome-wide CRISPR screens to understand the underlying biological principle and found that MSB depletes the early endosomal (EE) membrane lipid phosphatidylinositol 3-phosphate [PI(3)P]. PI(3)P defines the EE compartment, allowing sorting of derived vesicles back to the plasma membrane or into the lysosomal degradation system. Video microscopy revealed that the distinctive feature of triaptosis is the accumulation of large PI(3)P-negative, deidentified endosomes followed by cell blebbing and plasma membrane rupture. We found that MSB directly oxidizes essential cysteines on class III PI 3-kinase VPS34, thus inactivating the PI(3)P-producing enzyme. Notably, supplementing cells with extra reducing agents completely abrogates cell death induced by MSB. The ability of menadione to suppress PI(3)P production prompted us to test whether it could suppress a fatal inherited disorder: X-linked myotubular myopathy. This incurable disease is caused by inherited mutation of the *MTM1* gene. MTM1 is the phosphatase that directly antagonizes PI 3-kinase VPS34. Therefore, boys with this disease suffer from unopposed PI(3)P production, causing a failure of muscle buildup. *Mtm1* knockout mice recapitulate the most severe phenotype, lethality of infant boys. Supplementing MSB in drinking water doubled the overall survival of these mice to a median of 2 months. The treatment also improved animal weight gain and muscle histology.

CONCLUSION: Our results suggest that dietary menadione could form the basis of new therapeutic approaches in multiple disease settings. This is because MSB is an oxidative antagonist of PI 3-kinase VPS34, the enzyme that produces the phospholipid PI(3)P. In PC cells, the oxidative stress lowers PI(3)P, causing cell death by triaptosis. We infer from our data that normal cells have sufficient reserves in reducing power to withstand this insult. In myotubular myopathy, menadione may curb the unopposed VPS34 kinase activity and bring PI3P back to levels that can improve muscle development. Collectively, our findings contribute to the emerging understanding of pro-oxidant agent selectivity and show how definition of the pathways that they impinge on can give rise to unexpected therapeutic opportunities. ■

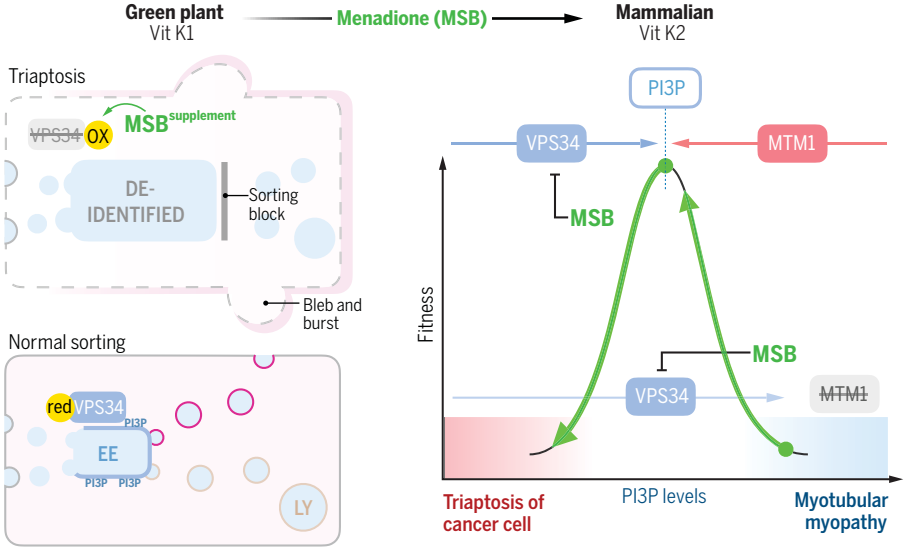

Dietary pro-oxidant therapy using a vitamin K precursor. (Top) Green plant foods are a major source of vitamin K (Vit K1), which mammals convert to Vit K2. The intermediate is menadione, which can be supplemented to diets (MSB). (Left) MSB oxidizes VPS34 kinase. This causes triaptosis, a distinct cell death mechanism based on depletion of PI3P, which deidentifies the EE compartment. LY, lysosomal degradation system. (Right) Concept of therapy approaches using PI3P reduction by MSB in two disease settings.

The list of author affiliations is available in the full article online.
***Corresponding author. Email: trotman@cshl.edu**
†These authors contributed equally to this work.
Cite this article as M. M. Swamynathan *et al.*, *Science* 386, eadk9167 (2024). DOI: 10.1126/science.adk9167

READ THE FULL ARTICLE AT
https://doi.org/10.1126/science.adk9167

RESEARCH ARTICLE

METABOLISM

Dietary pro-oxidant therapy by a vitamin K precursor targets PI 3-kinase VPS34 function

Manojit M. Swamynathan[1,2], Shan Kuang[1]†, Kaitlin E. Watrud[1]†, Mary R. Doherty[1]†, Charlotte Gineste[3], Grinu Mathew[1,4], Grace Q. Gong[5], Hilary Cox[1], Eileen Cheng[1], David Reiss[3], Jude Kendall[1], Diya Ghosh[1], Colleen R. Reczek[6], Xiang Zhao[1], Tali Herzka[1], Saulė Špokaitė[5], Antoine N. Dessus[5], Seung Tea Kim[1,2], Olaf Klingbeil[1], Juan Liu[7], Dawid G. Nowak[8,9,10], Habeeb Alsudani[1], Tse-Luen Wee[1], Youngkyu Park[1], Francesca Minicozzi[1], Keith Rivera[1], Ana S. Almeida[1,11], Kenneth Chang[1], Ram P. Chakrabarty[6], John E. Wilkinson[12], Phyllis A. Gimotty[13], Sarah D. Diermeier[14], Mikala Egeblad[1,15], Christopher R. Vakoc[1], Jason W. Locasale[7], Navdeep S. Chandel[6], Tobias Janowitz[1], James B. Hicks[1,16], Michael Wigler[1], Darryl J. Pappin[1], Roger L. Williams[5], Paolo Cifani[1], David A. Tuveson[1], Jocelyn Laporte[3], Lloyd C. Trotman[1]*

Men taking antioxidant vitamin E supplements have increased prostate cancer (PC) risk. However, whether pro-oxidants protect from PC remained unclear. In this work, we show that a pro-oxidant vitamin K precursor [menadione sodium bisulfite (MSB)] suppresses PC progression in mice, killing cells through an oxidative cell death: MSB antagonizes the essential class III phosphatidylinositol (PI) 3-kinase VPS34—the regulator of endosome identity and sorting—through oxidation of key cysteines, pointing to a redox checkpoint in sorting. Testing MSB in a myotubular myopathy model that is driven by loss of *MTM1*—the phosphatase antagonist of VPS34—we show that dietary MSB improved muscle histology and function and extended life span. These findings enhance our understanding of pro-oxidant selectivity and show how definition of the pathways they impinge on can give rise to unexpected therapeutic opportunities.

With an estimated 299,000 new diagnoses in 2024, prostate cancer (PC) remains the second most frequent tumor diagnosed in men and the second leading cause of male cancer deaths in the US (*1*). Therapeutic options for localized PC are effective; however, metastatic PC is a yet-incurable disease because standard-of-care antiandrogen therapy over time results in relapse of incurable disease. Therefore, there is much interest in how lifestyle and diet affect this slow-growing cancer. The SELECT trial (Selenium and Vitamin E Cancer Prevention Trial) followed around 35,000 men over the course of 10 years to test for benefits of dietary antioxidant supplements on risk of PC diagnosis. The trial unambiguously revealed the tumor-promoting not -reducing effects of antioxidants on PC (*2*, *3*). However, it has remained unclear whether, vice versa, pro-oxidant supplements are a viable strategy to stave off the disease. Therefore, we tested whether pro-oxidant therapy could protect from PC progression.

[1]Cold Spring Harbor Laboratory, Cold Spring Harbor, NY 11771, USA. [2]Graduate Program in Molecular and Cellular Biology, Stony Brook University, Stony Brook, NY 11794, USA. [3]Institut de Génétique et de Biologie Moléculaire et Cellulaire, CNRS UMR7104, Inserm U1258, Strasbourg University, Illkirch CEDEX 67404, France. [4]Eppley Institute, University of Nebraska Medical Center, Omaha, NE 68198, USA. [5]MRC Laboratory of Molecular Biology, Cambridge CB2 0QH, UK. [6]Department of Medicine, Feinberg School of Medicine, Northwestern University, Chicago, IL 60611, USA. [7]Department of Molecular and Structural Biochemistry, North Carolina State University, Raleigh, NC 27695, USA. [8]Department of Medicine, Meyer Cancer Center, Weill Cornell Medicine, New York, NY 10065, USA. [9]Department of Pharmacology, Weill Cornell Medicine, New York, NY 10065, USA. [10]Division of Hematology and Medical Oncology, Department of Medicine, New York Presbyterian Hospital, Weill Cornell Medicine, New York, NY 10065, USA. [11]APC Microbiome Ireland and School of Microbiology, University College Cork, Cork T12 K8AF, Ireland. [12]Department of Pathology, University of Michigan, Ann Arbor, MI 48109, USA. [13]Perelman School of Medicine, Division of Biostatistics, University of Pennsylvania, Philadelphia, PA 19104, USA. [14]Department of Biochemistry, University of Otago, Dunedin 9016, New Zealand. [15]School of Medicine, Johns Hopkins University, Baltimore, MD 21205, USA. [16]Michelson Center for Convergent Biosciences, University of Southern California, Los Angeles, CA 90089, USA.
*Corresponding author. Email: trotman@cshl.edu
†These authors contributed equally to this work.

Dietary MSB treatment suppresses PC progression

We used RapidCaP, an approach for somatic gene transfer of Cre-recombinase and luciferase transgenes into the prostates of *Pten*$^{loxP/loxP}$; *Trp53*$^{loxP/loxP}$ mice. This results in focal tumor initiation followed by lethal metastasis at high penetrance in a fully native environment (*4*–*6*). We monitored intensity and spread of PC by weekly bioluminescence imaging (BLI) to combine the rigor of genetically engineered mouse (GEM) models with an unbiased account of disease progression throughout the body. As pro-oxidants, we tested two approaches: (i) the vitamin K precursor menadione [also known as vitamin K3 (VK3)], administered in its water-soluble form, menadione sodium bisulfite (MSB), and (ii) the combination of MSB with vitamin C (VC). VC has been shown to oxidize cancer cells in vitro and in vivo (*7*–*10*). The selective uptake and intracellular reduction of dehydroascorbic acid in a GEM model for PC has been demonstrated using hyperpolarized magnetic resonance spectroscopy (*8*, *11*), and the combination with MSB has been proposed to enhance pro-oxidant function (*12*). Twenty-five animals with a spectrum of primary and metastatic disease burden as judged by BLI were enrolled and randomized into the three trial arms: water (10 animals), MSB (in drinking water at 150 μg/ml; 7 animals), or MSB plus VC (MSB & VC = MSB plus 1.5 mg/ml of sodium ascorbate; 8 animals). Treatments were prepared freshly from powder every day.

Imaging the three cohorts weekly for 18 weeks revealed that, in contrast to the steady disease progression in the water control group, the two treatment groups showed a marked treatment response, durable response, and no adverse weight change compared with water (Fig. 1, A and B, and fig. S1, A to C). This was in contrast to castration therapy of RapidCaP, where a treatment response is shorter than 60 days and invariably followed by castration resistance, as seen by sharp BLI increase and lethal disease progression (Fig. 1C) (*4*). One animal each in the MSB and the MSB & VC treatment groups also showed lethal 1300% and 1400% increase in disease burden (fig. S1, B and C), and they were confirmed as statistical outliers. In spite of the previously reported in vitro synergy (*12*), VC addition did not improve on MSB treatment in our hands. We measured VC and found no VC increase beyond endogenous levels in the liver and prostate of trial animals upon oral VC (fig. S2, A and B). Note that mice, like most mammals (but not humans), are able to generate their own VC. This finding suggested that high-dose injection of VC is critical to study its oxidative anticancer efficacy in mice, as has been published previously in prostate (*8*, *11*) and colorectal cancer (*9*). By contrast, liquid chromatography–mass spectrometry (LC-MS) analysis confirmed that the oral MSB treatment regimen delivered MSB to the prostate, where it acted as a pro-oxidant (Fig. 1D and fig. S2C). No effects on coagulation were seen upon oral MSB (fig. S2D).

We reasoned that the resistant tumors might contain valuable information on the underlying mechanisms behind both MSB-induced disease regression and resistance. Because the native tumors and metastases of the RapidCaP system are much smaller than those in humans, we could not simply harvest lesions for molecular probing. Instead, we turned to single-nucleus sequencing of whole-genome copy number alteration (CNA), the driving force behind PC evolution (*13*, *14*). Luciferase-guided harvesting of suspected tumor regions (fig. S2E, bottom)

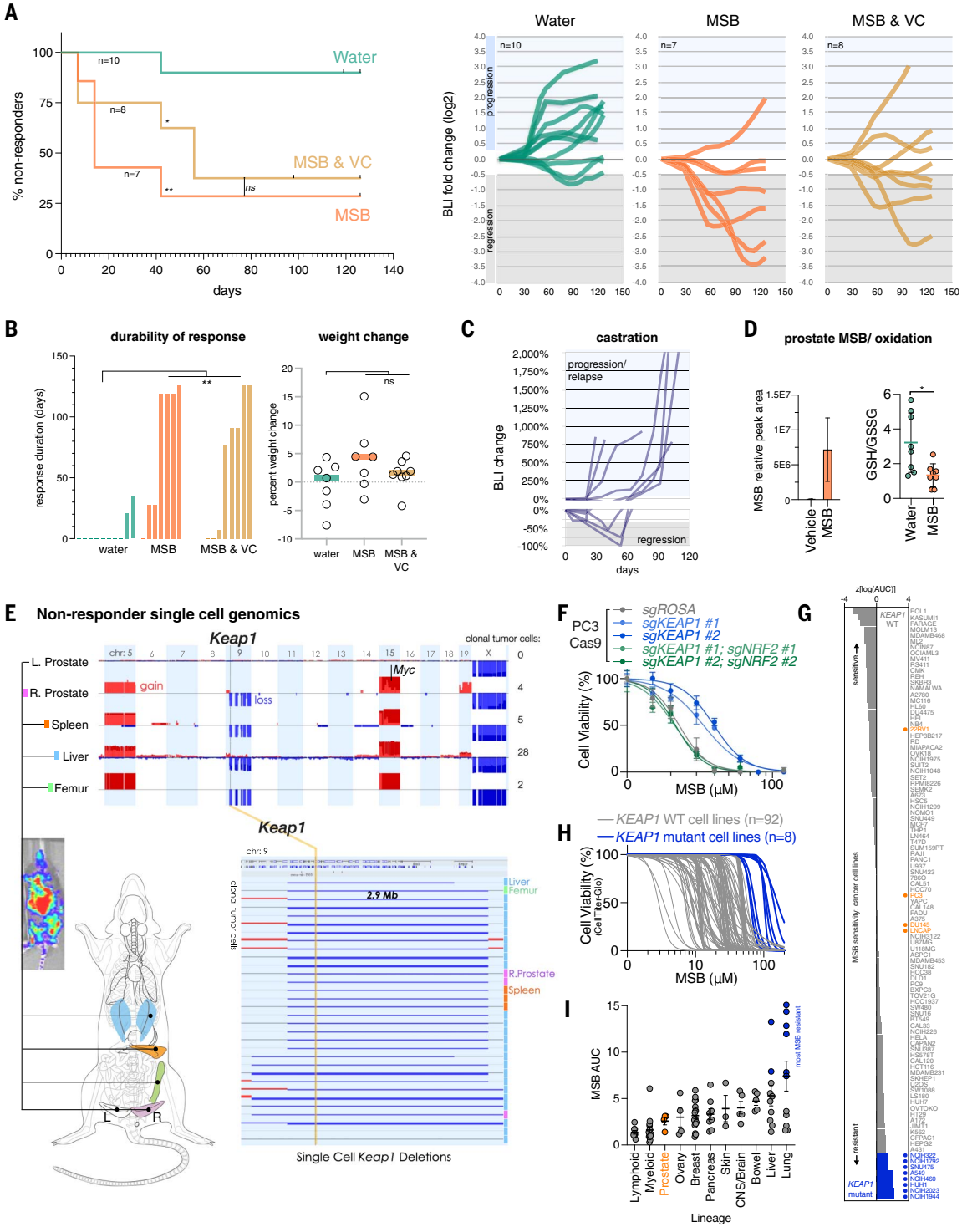

Fig. 1. MSB suppresses PC progression and induces oxidative stress. (**A**) (Left) Kaplan-Meier analysis of treatment response as defined by four consecutive BLI measurements showing partial response using RECIST criteria (at least 30% reduction in BLI; see also fig. S1A). *P* values were calculated using the Mantel-Cox test. ns, not significant; $*P < 0.05$; $**P < 0.01$. (Right) Line plots showing disease progression over time based on weekly $\log_2$ fold change in tumor BLI signal for each trial mouse (moving average of five consecutive measurements). Bounds based on RECIST criteria for regression (at least 30%) and progression (at least 20%) are indicated in gray and blue shading, respectively. Start- and endpoint BLI images and analyses are shown in fig. S1, A to C. (**B**) (Left) Durability of treatment response (at least 30% reduction) in the three trial arms. (Right) Percent weight change over 18 weeks (126 days). One-way analysis of variance (ANOVA) test for multiple comparisons of treatments versus water group was used. $**P < 0.01$; ns, not significant. (**C**) Reference RapidCaP trial for standard-of-care castration therapy, as published in (*4*), showing regression and relapse kinetics. (**D**) (Left) LC-MS analysis of MSB abundance in the prostates of animals treated with water or MSB ($n = 5$ biologically independent samples). (Right) Redox status indicated by the GSH/GSSG ratios in the prostates of mice treated with water ($n = 8$ biologically independent samples) or MSB ($n = 8$ biologically independent samples). Data are means ± SEMs (left) and means ± SDs (right). *P* values were calculated using two-tailed unpaired Student's *t* test. $*P < 0.05$. (**E**) Single-nucleus whole-genome CNA of a resistant RapidCaP clone that has metastasized from the prostate to the liver, spleen, and bone and harbors a deletion involving *Keap1*. See fig. S1C and fig. S2G for disease progression. (**F**) Cell viability curves for the indicated CRISPR-Cas9–derived isogenic human PC3 cell lines treated with increasing concentrations of MSB for 24 hours ($n = 3$ biologically independent samples). Data are means ± SDs. (**G**) Waterfall plot of z-scores of log(AUC) values, representing MSB sensitivities of 100 cancer cell lines. Blue indicates cancer cell lines with *KEAP1* loss-of-function, damaging, or hotspot mutations. PC cell lines are shown in orange. (**H**) Cell viability curves of the 100 cancer cell lines (gray, *KEAP1* WT; blue, *KEAP1* mutant) treated with increasing concentrations of MSB for 24 hours ($n = 3$ biologically independent samples). (**I**) Relationship between MSB potency and lineage for a subset of cancer cell lines tested in (H). Cancer cell types are ranked by their average MSB sensitivity. Blue indicates cancer cell lines with *KEAP1* loss-of-function, damaging, or hotspot mutations. PC cell lines are shown in orange. Data are means ± SEMs.

followed by fluorescence-activated cell sorting (FACS) of 4′,6-diamidino-2-phenylindole (DAPI)–stained nuclei allowed us to isolate 414 single nuclei from five tissues of an MSB-resistant animal: the left anterior prostate (normal control lobe), right anterior prostate (tumor-containing lobe), femur, spleen, and liver. These were subjected to single-nucleus whole-genome sequencing (SNS) to identify and characterize the cancer cells, as previously published for human PC samples (*15*, *16*). The genomes at each site included many tumor-diluting putative normal cells (0% CNA), just like the normal left anterior prostate (fig. S2E). By contrast, the right anterior prostate (origin of disease in RapidCaP) and the luciferase-positive metastatic sites also harbored cells with significantly ($P < 0.0001$) increased spontaneous CNA (note that the Cre-mediated *Pten* and *Trp53* deletions are below our CNA detection limit of 600 kb). This resembled the principle of progression first shown in human PC (*13*). Furthermore, analysis of all 414 single-nucleus genomes also revealed cells with recurrent CNA (fig. S2F). Focus on 60 cancer cells with clonal CNA revealed increasing degrees of complexity: prostate < spleen < liver, potentially delineating a route of metastasis (fig. S2, G to I). As shown in Fig. 1E, the cancer clone featured two whole-chromosome gains, including *Myc* on chromosome 15 as published previously (*4*), and five deletions on chromosome 9, of which two were focal [smaller than 3 mega–base pairs (Mbp)]. One of these deletions contained the *Keap1* gene, a tumor suppressor and master sensor of oxidative stress (*17*, *18*).

We confirmed increased tolerance to MSB in *Keap1*$^{-/-}$ mouse embryonic fibroblasts (MEFs) and using CRISPR-Cas9 in human PC3 and LNCaP, consistent with an increase in redox buffering capacity (Fig. 1F and fig. S3, A to C). Next, we individually tested 100 cancer cell lines from our institute (data S1) for sensitivity to MSB. We found that specifically those with known preexisting loss-of-function *KEAP1* mutations were most MSB resistant (Fig. 1, G and H), and our query of the Broad's DepMap 23Q2 dataset for gene essentiality (*19*) suggested that the top genetic dependency specific to the MSB-resistant cell lines is the oncogenic transcription factor NRF2 (encoded by *NFE2L2*), which is suppressed by KEAP1 (fig. S3, D to F). We confirmed this imputed connection to MSB using CRISPR-Cas9: Human LNCaP and metastasis-derived PC3 cells become more MSB tolerant after loss of *KEAP1*, but cotargeting of *NRF2* ablates this effect, consistent with the epistatic genetic relationship (Fig. 1F and fig. S3, C, G, and H). A metastatic subclone harboring amplification of NRF2 (*Nfe2l2* gene) was found by SNS analysis of a liver and lung metastasis in a nonresponder animal (fig. S3I).

Our experiment in a preclinical GEM model for metastatic PC revealed (i) a marked reduction of disease progression upon prolonged oral MSB administration and (ii) that unlike with castration therapy in RapidCaP, lethal therapy resistance was rare with MSB. And genomics revealed (iii) that therapy resistance may be controlled by the KEAP1-NRF2 antioxidant system, which suggests that cancer cells were under oxidative selection pressure. Because human PC cell lines rank among the most MSB sensitive by lineage (Fig. 1I), and because the KEAP1-NRF2 pathway is rarely altered in human PC (*14*), we reasoned that there should be little a priori genetic resistance to MSB. Therefore, we sought to better understand how exactly MSB acts on cancer cells.

MSB triggers a thiol-dependent cell death modality

As in the prostate (Fig. 1D), MSB also caused glutathione (GSH) depletion in vitro (Fig. 2A and fig. S4A) and increased cytoplasmic reactive oxygen species (ROS) levels (Fig. 2B). We therefore tested cell-autonomous mechanisms underlying the MSB effect. As suspected, cell viability inversely correlated with cell death, and this MSB-kill was effectively prevented by supplementing GSH or its precursor N-acetylcysteine (NAC) but not downstream cysteine metabolites (fig. S4, B and C). Preincubation of the strongly cell-permeable GSH ethyl ester effectively desensitized cells to MSB, confirming that reductive protection happens inside the cell (fig. S4D). To quantify and compare protective versus sensitizing effects of modulators on MSB-kill, we calculated changes in normalized area under the curve (ΔAUC_n; diagram in fig. S4E) and generated ΔAUC_n heatmaps ordered by unsupervised hierarchical clustering. This approach allowed us to comprehensively and quantitatively summarize properties of MSB-kill. Thus, the kill curves of cysteine metabolite effects from fig. S4C are succinctly captured with a heatmap, as shown in Fig. 2C.

We next tested whether MSB engages a discrete death pathway because previous literature has implicated multiple redundant and also mutually exclusive cell death pathways (*20*–*22*). Several observations prompted us to first test whether MSB acts through perturbation of the mitochondrial electron transport chain (ETC): The plant K-vitamer phylloquinone (VK1; fig. S4F) is essential in photosystem I of the chloroplast ETC (*23*). Ubiquinone, the mitochondrial electron carrier, is structurally related to the K-vitamer menaquinone (VK2; fig. S4F), and *Pten* and/or *Trp53* mutant PC cells are vulnerable to mitochondrial complex I inhibition (*24*–*27*). Yet, we found that MSB-kill was not suppressed by yeast NDI1, a rescue transgene for mitochondrial complex I inhibitors (*28*), and MSB did not induce mitochondrial ROS (fig. S4, G to I).

We next screened drugs with known cytotoxic mechanisms (fig. S5A) to determine whether any of them share properties with MSB, using the CRISPR-derived isogenic *KEAP1* mutant PC3 cells (Fig. 2D). Clustering analysis of this screen revealed that only 3 of 40 cytotoxic agents were similar to MSB: H_2O_2 as well as erastin and RSL3, two inducers of ferroptosis (*29*, *30*). Additionally, we confirmed that the transcriptome changes upon MSB and erastin were strongly correlated (fig. S5B). Thus, to pharmacologically define the cell death pathway engaged by MSB more precisely, we used a process called modulatory profiling (*31*, *32*). Three well-known modalities of cell death (apoptosis, programmed necrosis, and ferroptosis) were triggered and then blocked using their respective pathway-specific modulators (see data S2 for more information and expected mechanism). The resulting signatures were compared with that of MSB. As shown in Fig. 2E, pan-caspase inhibitors z-VAD-fmk and qVD-oph selectively protected from staurosporine-induced apoptosis but conferred no protection from MSB-kill. *Bax*$^{-/-}$;*Bak*$^{-/-}$ MEFs remained MSB sensitive, and we found no caspase activation, adenosine 5′-triphosphate (ATP) depletion, or autophagosome accumulation (fig. S5, C to E). H_2O_2-mediated programmed necrosis was suppressed by replenishing the oxidized form of nicotinamide adenine dinucleotide (NAD^+) using alternative electron acceptors (AKB and EP) or the poly(ADP-ribose) polymerase (PARP) inhibitor DPQ (*9*, *33*) and by the intracellular calcium chelator BAPTA-AM. Erastin-induced ferroptosis was suppressed effectively by lipid ROS scavenger ferrostatin-1, the iron chelator desferoxamine (DFO), the lysosomal inhibitor bafilomycin A-1, or GSH (Fig. 2E). However, MSB-kill did not share any of the signatures with the above cell death modalities (Fig. 2E, bottom row). GSH was the only functional modulator that it shared with erastin. Together, these findings suggest that MSB killed cells through a specific type of oxidative stress that was unaffected by key modulators of ferroptosis, like ferrostatin-1. This was confirmed in human- and mouse-derived PC cells (fig. S5F).

We further tested how compartmentalized oxidative stress induction compared with MSB using phenformin (mitochondria), chloroquine (lysosomes), and doxorubicin (nucleus), and each was rescued by their known respective modulators (Fig. 2E). However, none of these suppressed MSB-kill, and, vice versa, GSH only prevented MSB-kill but not death by these other oxidants. This suggested that MSB can target a distinct thiol-sensitive cell death pathway.

To better understand this thiol-selective pathway, we tested the effects of 11 known redox modulators on MSB toxicity and on four other pro-oxidant compounds. As shown in Fig. 2F, staurosporine served as a negative control compound for the 11 modulators. Buthionine sulphoximine (BSO), an inhibitor of GSH production,

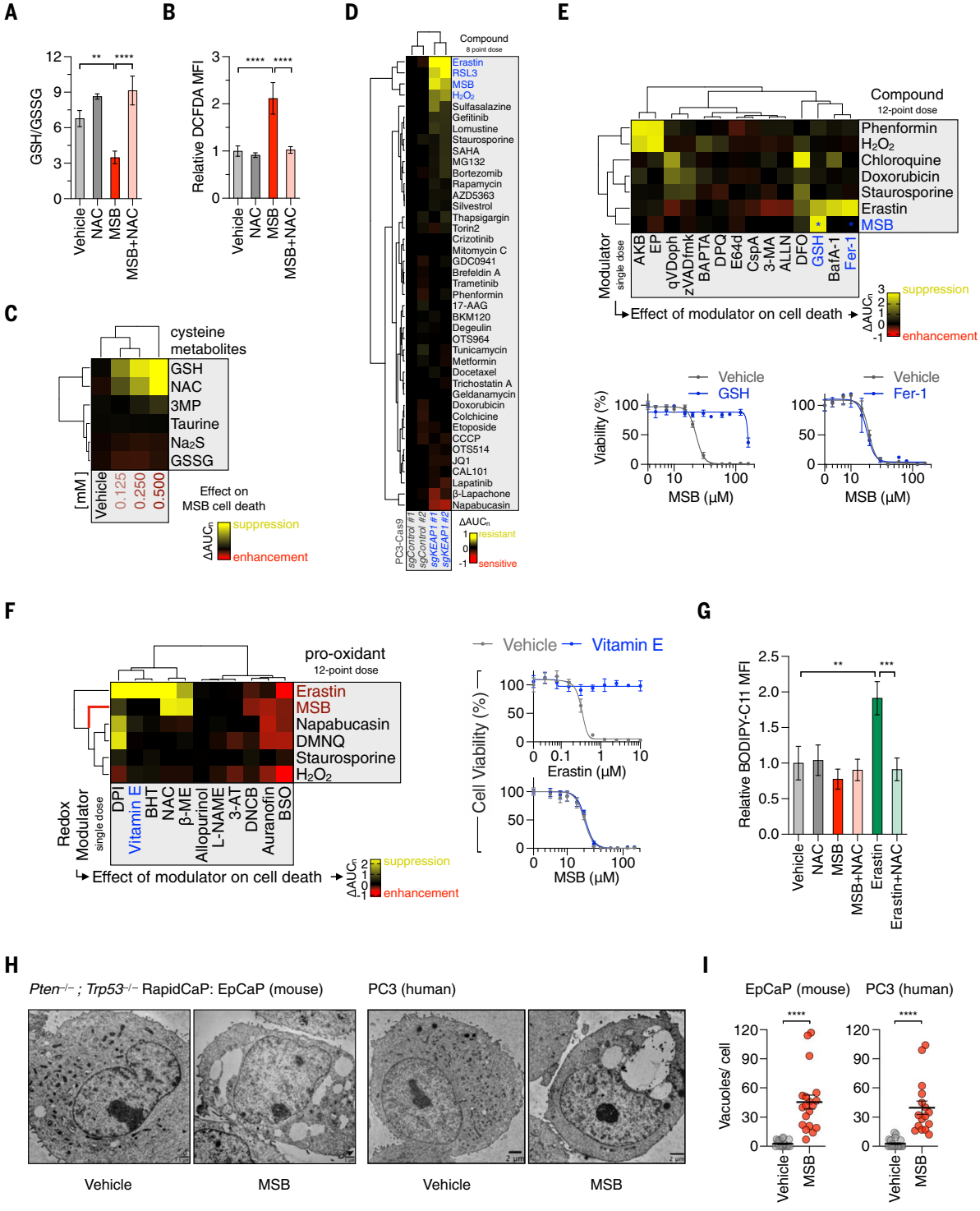

Fig. 2. MSB triggers an oxidative cell death modality. (**A**) GSH/GSSG ratios (n = 3 biologically independent samples). (**B**) Cytoplasmic ROS levels quantified by staining of CM-H2DCFDA followed by flow cytometry (n = 3 biologically independent samples) in vehicle, NAC (0.5 mM), MSB (20 μM), or MSB+NAC treated *Pten*$^{-/-}$;*Trp53*$^{-/-}$ MEFs, 4 hours after treatment. Data are means ± SDs. P values were calculated using one-way ANOVA. $^{**}P < 0.01$; $^{****}P < 0.0001$. (**C**) Heatmap plotting ΔAUC_n values depicts the extent of protection conferred by different cysteine metabolites from MSB-induced cell death. $\Delta AUC_n > 0$ or yellow color indicates that the respective cysteine metabolite protects from MSB-induced cell death. (**D**) A heatmap of the differential sensitivities for 40 compounds (rows) in the CRISPR-Cas9–derived isogenic PC3 cell lines (columns). $\Delta AUC_n > 0$ (or yellow) indicates increased resistance and $\Delta AUC_n < 0$ (or red) indicates increased sensitivity to a particular compound. $\Delta AUC_n = 0$ (or black) indicates no differential sensitivity between the isogenic cell lines. Erastin, RSL3, MSB, and H_2O_2 (indicated in blue) are grouped together through unsupervised hierarchical clustering analysis. (**E**) (Top) Modulatory profiling depicting the effect of 14 cell death modulators (columns) on MSB-induced cell death or other distinct cell death pathways induced by the indicated compounds (rows) in *Pten*$^{-/-}$;*Trp53*$^{-/-}$ MEFs. $\Delta AUC_n > 0$ (or yellow color) indicates a protective effect of the modulator from the cell death pathway or compound,

whereas $\Delta AUC_n < 0$ (or red color) indicates that the given modulator renders cells more sensitive to the cell death pathway or compound. $\Delta AUC_n = 0$ (or black color) indicates that the given modulator has no effect on the cytotoxic effect of the compound. (Bottom) Viability curves of *Pten*$^{-/-}$;*Trp53*$^{-/-}$ MEFs treated with increasing concentrations of MSB for 24 hours, alone or in combination with GSH (0.5 mM; left) or ferrostatin-1 (2.5 μM; right) (n = 3 biologically independent samples). Data are means ± SDs. (**F**) (Left) Modulatory profiling depicting the effect of 11 redox or ROS modulators (columns) on toxicity induced by MSB, other pro-oxidative, or nonoxidative compounds (rows) in *Pten*$^{-/-}$;*Trp53*$^{-/-}$ MEFs. (Right) Viability curves of *Pten*$^{-/-}$;*Trp53*$^{-/-}$ MEFs treated with increasing concentrations of erastin (top) or MSB (bottom) for 24 hours, alone or in combination with the lipophilic antioxidant vitamin E (100 μM) (n = 3 biologically independent samples). Data are means ± SDs. (**G**) Production of lipid ROS measured and quantified by staining of C11-BODIPY 6 hours after vehicle, NAC (0.5 mM), MSB (20 μM), NAC+MSB, erastin (0.3 μM), or erastin+NAC treatment in *Pten*$^{-/-}$;*Trp53*$^{-/-}$ MEFs followed by flow cytometry (n = 3 biologically independent samples). Data are means ± SDs. P values were calculated using one-way ANOVA. $^{**}P < 0.01$; $^{***}P < 0.001$. (**H**) TEM images of *Pten*$^{-/-}$;*Trp53*$^{-/-}$ EpCaP cells (left; scale bar, 1 μm) or PC3 cells (right; scale bar, 2 μm) upon vehicle or MSB (30 μM) treatment. (**I**) Quantification of the number of enlarged vesicles in EpCaP cells (left) or PC3 cells (right) treated with vehicle or MSB (30 μM). Data are means ± SDs. P values were calculated using two-tailed unpaired Student's t test. $^{****}P < 0.0001$.

generally sensitized cells to all five pro-oxidant compounds (erastin, MSB, napabucasin-BBI608, 1-chloro-2,4-dinitrobenzene or DMNQ, and H_2O_2), whereas DNCB (an inhibitor of thioredoxin reductase) was more MSB-specific. Conversely, the NADPH oxidase (NOX) inhibitor diphenyleneiodonium chloride (DPI) protected from four of the five pro-oxidants, albeit only weakly for MSB. Clustering analysis of the modulators revealed two critical differences between erastin and MSB. Most notably, vitamin E (α-tocopherol), the specific inhibitor of lipid peroxidation, blocked ferroptosis by erastin, but it had no effect on MSB-kill (Fig. 2F, heatmap and kill curves). Another lipophilic antioxidant, dibutylated hydroxytoluene (BHT), also selectively rescued from erastin but not from MSB. This was in contrast to the thiol-reducing agents NAC and β-mercaptoethanol (β-ME). The findings were confirmed in human- and mouse-derived PC cells (fig. S5F). Most notably, we found that in contrast to erastin, MSB did not cause lipid peroxidation, the defining feature of ferroptosis, as seen using flow cytometry analysis of the membrane lipid ROS reporter BODIPY-C11 (Fig. 2G).

Finally, we used transmission electron microscopy (TEM) to analyze morphological features of MSB-induced cell death in human PC3- and RapidCaP-derived epithelial PC cells (EpCaP). This revealed a significant ($P < 0.0001$) buildup of cytoplasmic vacuoles (Fig. 2, H and I, and fig. S5G); however, we did not note features of classical cell death pathways, such as chromatin condensation (*34*). Taken together, our analyses suggest that MSB kills through an oxidative cell death mechanism that shares biochemical and genetic features with ferroptosis—such as thiol depletion and *KEAP1* dependence—but is independent of lipid peroxidation and is morphologically distinct.

Genome-wide screens for functional regulators of MSB-kill

To distinguish events that are causal to MSB-kill from those that are merely correlated, we decided to (i) use CRISPR-Cas9 screens that nominate functionally relevant genes of MSB-kill, (ii) perform the screens genome-wide so that underlying principles are more objectively revealed than by focused pathway screens, and (iii) perform both positive and negative selection screens that approach the question from opposite sides. A sensitization screen administered sublethal MSB to identify gene alterations that only become detrimental upon exposure to EC_{10} (effective concentration to obtain a 10% effect) ("MSB^{low}"; negative selection). A resistance screen was also done to identify gene alterations that confer a survival advantage to a high concentration (EC_{50}) ("MSB^{high}"; positive selection). Both screens compared the fitness effect of the gene perturbation plus vehicle with that of gene perturbation plus MSB. We used the Broad Institute's Brunello whole-genome single-guide RNA (sgRNA) library of 76,441 sgRNAs targeting 19,114 human coding genes (four sgRNAs per gene) and 1000 control sgRNAs in the human metastasis–derived PC3 cell line.

Gene ontology analysis of the leading-edge hits in the sensitizing screen (MSB^{low}) revealed genes mediating endocytosis (Fig. 3A, fig. S6A, and data S3): endophilin A3 (*SH3GL3*), which mediates fast endophilin-mediated endocytosis (FEME) [(*35*), reviewed in (*36*)], as well as effectors of macropinocytosis and membrane ruffling (*ELMO2*, *NCKAP1*, *ACTN2*, and *KXD1*). Gene ontology analysis of the MSB^{high} positive selection screen showed enrichment specifically for late endosome associated genes (fig. S6, B and C). These included RAB7–guanosine triphosphatase (GTPase) effectors of late endosomal trafficking (*WDR91* and *FYCO1*), maturation (*RAB9A*, *SCARB2*, and *ANXA8*), and acidification (*CLCN4* and *ATP13A2*; data S3), suggesting that their loss increased tolerance to MSB. Together, these data suggested that cell kill by MSB is functionally linked to endocytosis. More specifically, it suggested that inhibiting early steps of endocytosis and endosome formation could support MSB-kill, whereas inhibiting late endosomal progression could suppress MSB-kill.

We noted that VPS15 was among the leading-edge sensitizing CRISPR hits (Fig. 3A, *PIK3R4* gene). This stood out because VPS15 is a component of the endosomal class III phosphatidylinositol (PI) 3-kinase VPS34 complex (*37*). This complex defines the cell's early endosomal (EE) compartment by marking it with the phosphatidylinositol 3-phosphate, PI(3)P lipid [reviewed in (*38*)]. This compartment is the central hub for endocytic routes as they are being funneled through it. Notably, the MTM1 phosphatase was in the leading edge of the MSB resistance screen. This phosphatase is the direct antagonist of endosomal VPS34 kinase (*39*) (Fig. 3A) because it reverts PI(3)P back into PI. This immediately suggested that a single enzyme-regulated reaction step could be at the core of MSB-kill: production versus elimination of the lipid phosphatidylinositol 3-phosphate [PI(3)P] (Fig. 3A, cartoon) (*40*). We therefore tested this hypothesis.

First, we validated these two screen hits using two independent domain-focused sgRNAs in three human primary and metastatic PC cell lines. Competition assays confirmed that CRISPR targeting of VPS15 (encoded by *PIK3R4*) confers sensitivity to MSB-kill compared with control guides. By contrast, targeting of *MTM1* boosted tolerance to MSB (Fig. 3, B and C, and fig. S6, D to J). Next, we validated that class III PI 3-kinase VPS34 (*PIK3C3* gene) function is essential in three PC cell lines using two independent sgRNAs targeting the kinase domain (fig. S7, A and B). CRISPR targeting of *MTM1* rescued the cells (at least in part) from the deleterious effect of *PIK3C3* ablation, in line with the enzymatic antagonism of this kinase-phosphatase pair (fig. S7C).

VPS34 kinase initiates autophagy through complex I, whereas complex II establishes the endosomal compartment (*37*). We found that MSB inhibited both autophagic flux (fig. S7D) and resulted in stalled endocytic uptake of extracellular dextran dye (Fig. 3D and fig. S7, E to G), consistent with the TEM results (Fig. 2H). The genome-wide CRISPR database on more than 1000 cancer cell lines curated at the Broad Institute (DepMap, 23Q2) showed that the proteins specific to the endosomal VPS34 complex II are top correlates to VPS15 genome-wide: *PIK3C3*, followed by *UVRAG* and *BECN1* (Fig. 3E). Notably, UVRAG is cell essential and exclusive to the endocytosis complex (II). By contrast, the autophagy complex exclusive ATG14 is nonessential and did not correlate with VPS15 (Fig. 3, E and F). This was consistent with our screen results: Although gene alterations involving thiol metabolism, ROS detoxification, and oxidoreductase pathways were

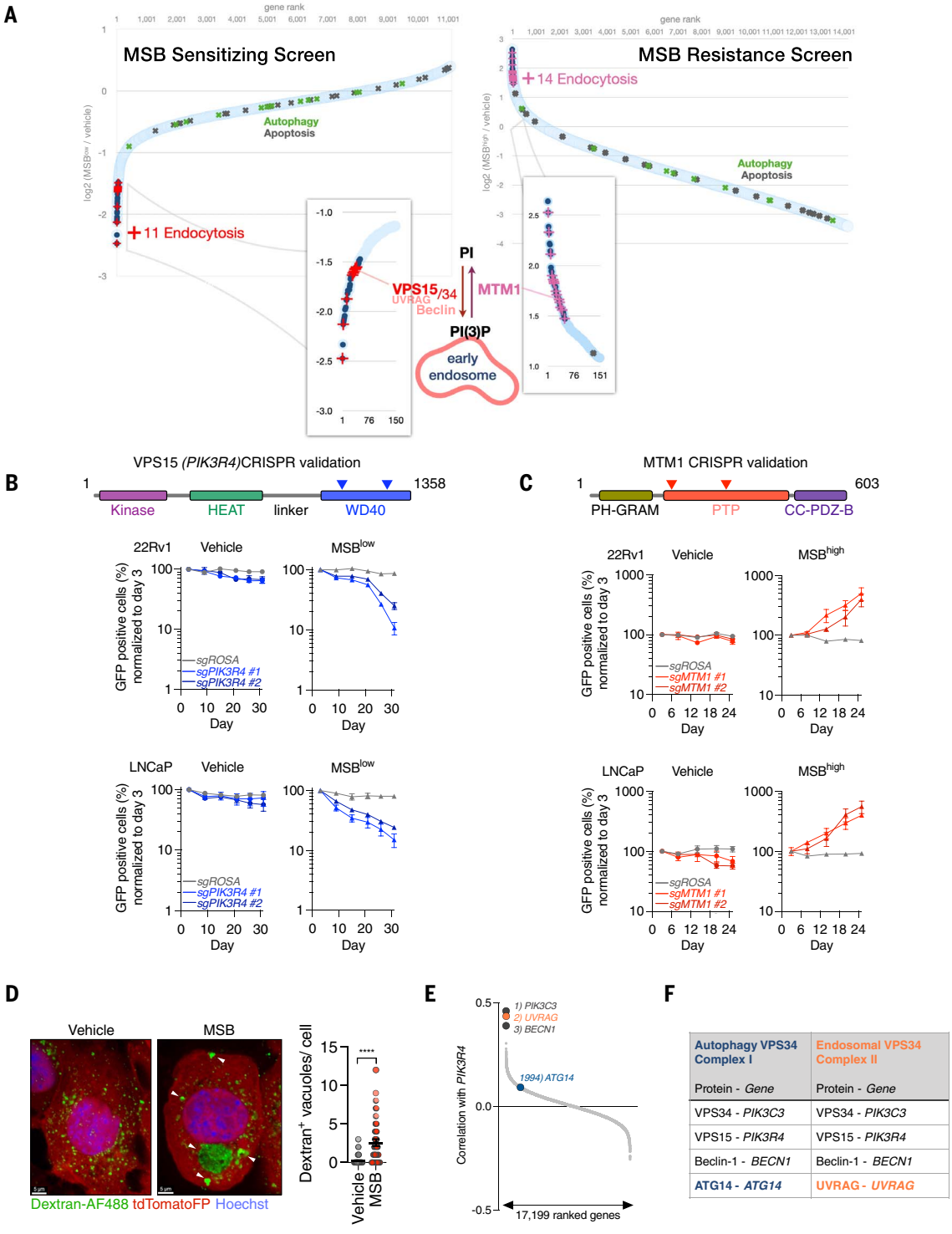

Fig. 3. Genome-wide functional regulators of MSB-kill. (**A**) Genome-wide CRISPR screens showing $\log_2$ fold change in abundance for genes upon MSB versus vehicle treatment in PC3-Cas9 cells. Gene-ranked leading edge and lagging tail of the sensitizing screen at 15 μM MSB and of the resistance screen at 30 μM MSB are shown left and right, respectively (light blue circles in background). Inserts show endocytosis regulators (red and purple crosses) among the top 50 (dark blue circles). Core apoptosis and autophagy genes are marked as green and gray crosses, respectively. The role of VPS15 in generating early endosome identity as part of the VPS34 complex and its antagonist, MTM1, is drawn. (**B**) (Top) Domain architecture of human VPS15 (encoded by *PIK3R4*). Locations of domain targeting sgRNAs are shown (arrowheads). (Bottom) Competition assay in indicated human PC cells stably expressing Cas9. Data are means ± SEMs; $n = 4$ biologically independent samples. (**C**) CRISPR design and results for validation of *MTM1* gene targeting, shown as in (B). (**D**) (Left) Confocal images of RapidCaP-derived cells stably expressing tdTomatoFP (red), fixed after 4 hours of treatment with vehicle or MSB (15 μM). The cells were cultured in medium supplemented with fluorescein-dextran (3 kDa) for the duration of the treatment. Arrowheads point to dextran-positive vacuoles. Scale bar, 5 μm. (Right) Quantification of the number of dextran-positive vacuoles per cell after 4 hours of treatment with vehicle ($n = 47$ cells) or MSB ($n = 49$ cells). Data are means ± SEMs. *P* values were calculated using two-tailed unpaired Student's *t* test. ****$P < 0.0001$. (**E**) 17,199 genes ranked based on the correlation of their essentiality profile with that of *PIK3R4* in 1095 cancer cell lines using CRISPR screening data from the Broad's DepMap database (23Q2). (**F**) Summary of protein and gene constituents of VPS34 complex I and II. The complex I–exclusive and complex II–exclusive genes are highlighted.

validated synergy hits with MSB (fig. S7, H to J), hallmark genes of autophagy, apoptosis, and other prominent cell death pathways were not (Fig. 3A and data S3). Taken together, these results led us to hypothesize that the endosomal PI 3-kinase VPS34 complex is a functional target of MSB-kill (Fig. 3A, cartoon) and that MSB controls class III PI 3-kinase VPS34 indirectly or directly in a redox-sensitive manner.

Endosomal class III PI 3-kinase VPS34 is a functional target of menadione-kill

We first used time-lapse microscopy to test the hypothesis that menadione kills cells by oxidative suppression of the endosomal VPS34-kinase complex. This allowed us to observe and quantify the steps that lead to cell death in greater detail. To this end, we generated epithelial nonmigratory PC cells derived from a RapidCaP (*Pten*$^{-/-}$;*Trp53*$^{-/-}$) tumor (EpCaP cells) to enable cell death imaging over a 24-hour period. The cells express tdTomatoFP representing cytosol and revealing obvious changes in the cytoplasm.

First, we recorded the cell death induced by the class III selective PI 3-kinase VPS34 inhibitor, VPS34-IN1 (*41*). As shown in Fig. 4A and the associated movies S1 and S2, we noted three separate events upon VPS34-IN1 treatment: cytoplasmic vacuolization, steadily intensifying plasma membrane (PM) blebbing, and terminal burst of cells as seen by complete loss of the tdTomatoFP cytosolic marker. To statistically compare this sequence of events, onset of vacuolization and time to burst were charted as Kaplan-Meier plots. As shown (Fig. 4B), vehicle treatment caused few background burst and vacuolization events. Notably, vacuolization followed by cell death are the phenotypes observed upon genetic VPS34 *Pik3c3* loss as studied by others (*42*, *43*) and us (*44*) in MEFs using the Cre-loxP system. Adding the NAC reducing agent to the kinase inhibitor did not change the kinetics, the extent of vacuolization, or burst events (Fig. 4B, VPS34-IN1 + NAC; movie S3; and fig. S8A). Analysis of MSB (Fig. 4, C and D, and movies S4 and S5) showed that it closely phenocopied the VPS34-IN1–induced vacuolization, blebbing, and burst sequence of events. But, in strong contrast, reduction with NAC eliminated vacuolization and PM bursts to background levels (Fig. 4D, MSB + NAC; fig. S8A; and movies S4 and S5). Next, we tested whether menadione inhibits class III PI 3-kinase VPS34 function of generating the PI(3)P marker on endosomes. The cells imaged in Fig. 4, A to D, are also transgenic for GFP-2xFYVE, the commonly used reporter (*45*) for PI(3)P, allowing us to determine whether and when PI(3)P was affected. As expected (Fig. 4E), the typical GFP-2xFYVE punctate signal was sharply reduced by the kinase inhibitor VPS34-IN1, indicating loss of PI(3)P-positive vesicles. MSB had a similar albeit slower effect, also before overt vacuolization, as seen in the imaging and quantification (Fig. 4, E and F; fig. S8B; and movies S6 to S9). The addition of NAC to MSB eliminated the effect on GFP-2xFYVE puncta, making it indistinguishable from vehicle treatment (fig. S8B). To test whether the cell death phenotypes were generalizable beyond the *PTEN* and/or *TP53* mutant background and beyond PC, we went through our results from MSB-kill in 100 cancer cell lines (Fig. 1, H and I) and used five sensitive cell types from unrelated cancers. This showed that burst was also preceded by vacuolization and that the process was thwarted by NAC (fig. S8C). Note that xFP or other cytosol markers are needed to report integrity of cells before PM burst at the time of fixation and permeabilization. Quantitative immunofluorescence in the PC3 cells validated that MSB, like VPS34-IN1, reduced PI(3)P-positive vesicles at both the MSB^{low} and the MSB^{high} screen concentrations, producing a diffuse cytoplasmic GFP-2XFYVE signal (Fig. 4G and fig. S9A). CRISPR targeting of VPS34 kinase phenocopied these effects of MSB and VPS34-IN1 (Fig. 4G and fig. S9A).

The small GTPase RAB5 recruits and activates VPS34 complex II on early endosomes (*46*) [see Fig. 4H, cartoon, and (*37*, *38*) for reviews], so we next tested whether MSB interferes with the positioning of RAB5a. However, we found abundant RAB5a decoration of MSB-induced vacuoles indistinguishable from pharmacological inhibition (VPS34-IN1) and genetic targeting of PI 3-kinase VPS34 (*PIK3C3*) in human and mouse cells using CRISPR-Cas9 and Cre-loxP, respectively (Fig. 4I and fig. S9, B and C). We next compared MSB effects with PIKFYVE inhibition. PIKFYVE converts PI(3)P on early endosomes to PI(3,5)P_2 for endo-lysosomal progression. PIKFYVE inhibition results in large vacuoles marked by late endosomal protein lysosomal-associated membrane protein 1 (LAMP1). By contrast, MSB- or VPS34-IN1–treated cells presented LAMP1-negative vacuoles, as shown in fig. S10A. Class II PI 3-kinases generate PI(3)P at the PM. Pharmacological targeting and screen analysis indicated that they offer no major protection from MSB-kill, consistent with dominant PI(3)P production by the class III kinase VPS34 (*38*). At the same time, MSB did not perturb *PIK3C2A* function (fig. S10, B to E).

Together, our results thus far supported two major conclusions: MSB can kill cells by indirectly or directly antagonizing endosomal PI 3-kinase VPS34, and this regulation is under redox control. Mechanistically, MSB-induced stalling of endocytosed vesicles is likely because two major downstream processing pathways depend on endosomal PI(3)P deposition onto RAB5-positive vesicles for coincident detection: Recycling to the PM requires PI(3)P on vesicles that is to be converted to PI(4)P, whereas progression into the endo-lysosomal degradative pathway requires first recognition then conversion of PI(3)P into PI(3,5)P_2 [reviewed in (*38*)]. Thus, our data hinted at the existence of a redox checkpoint at the stage of endosomal identification.

MSB oxidizes cysteines required for endosomal VPS34 function and survival

To test whether MSB oxidizes PI 3-kinase VPS34, we immunoprecipitated the kinase from MSB- or vehicle-treated cells (notably, MSB did not affect VPS34 levels, as seen in fig. S10F). We then subjected it to a sequential alkylation and reduction process that reveals cysteine modification states by MS (fig. S11A). As shown in Fig. 5A and fig. S11, B to D, we recovered 9 of a total 11 VPS34 cysteines and found that in peptide 1 (Cys^{54} or Cys^{61}) and peptide 2 (Cys^{226}), MSB caused a depletion in free thiol and a concomitant increase in reversible oxidation. Catalytic domain cysteines and negative control peptides were among the unaffected. Peptide 1 (Cys^{54} or Cys^{61}) maps to the C2 domain, which controls formation and function of the hetero-tetrameric VPS34 complex (*47*) and has been proposed as a hub for posttranslational control of VPS34 (*48*). We confirmed, using recombinant-purified VPS34 complexes in adenosine 5′-diphosphate (ADP) Glo kinase assays (*49*, *50*), that the activities of full-length VPS34, VPS34 complex I (CI), and VPS34 complex II (CII) were all inhibited by MSB (fig. S11E).

We then tested whether these VPS34 candidate cysteines could control cell viability. To this end, we performed gene knockout–plasmid rescue experiments using the VPS34 (*Pik3c3*$^{loxP/loxP}$) conditional knockout MEFs. These were stably transduced with the candidate VPS34 mutants carrying cysteine to alanine or cysteine to aspartate substitutions. The latter served as bona fide oxido-mimetic missense mutations. Upon infection with Cre.GFP lentivirus, the endogenous VPS34 was lost, and the fitness of the VPS34 mutant rescue plasmids was scored as the fraction of GFP-positive cells in each condition. Figure 5B (empty vector) shows that recombination of the endogenous VPS34 without replacement strongly depleted these cells (fig. S11F). By contrast, the VPS34 wild-type (WT) plasmid effectively rescued the *Pik3c3*$^{\Delta/\Delta}$ cells. Notably, all mutants of Cys^{54} and Cys^{61} were unable to rescue cells. This suggested (i) that these two cysteines are essential for VPS34 function and (ii) that their oxidation could inactivate the kinase complex. By contrast, the Cys^{226} mutants remained functional.

Finally, we assessed whether mutation of these cysteines recapitulates inactivation of endosomal VPS34 complex II by analyzing the cellular phenotypes. As shown in Fig. 5C (and fig. S12A), the Cys^{54} and Cys^{61} mutants showed strong RAB5-positive vacuole formation (compare with fig. S9). Thus, the mutants gave rise to the hallmark of MSB-kill, without MSB.

Collectively, our analysis showed that Cys^{54} and Cys^{61}, which can be reversibly oxidized by MSB, are required for endosomal VPS34 function. Therefore, they are strong candidates for an evolutionarily conserved redox switch on VPS34 (fig. S12B) that controls the oxidative cell death caused by MSB.

Dietary menadione extends life span in a fatal disease driven by PI 3-kinase VPS34

Because MSB antagonizes PI 3-kinase VPS34, we next tested whether it can effectively suppress

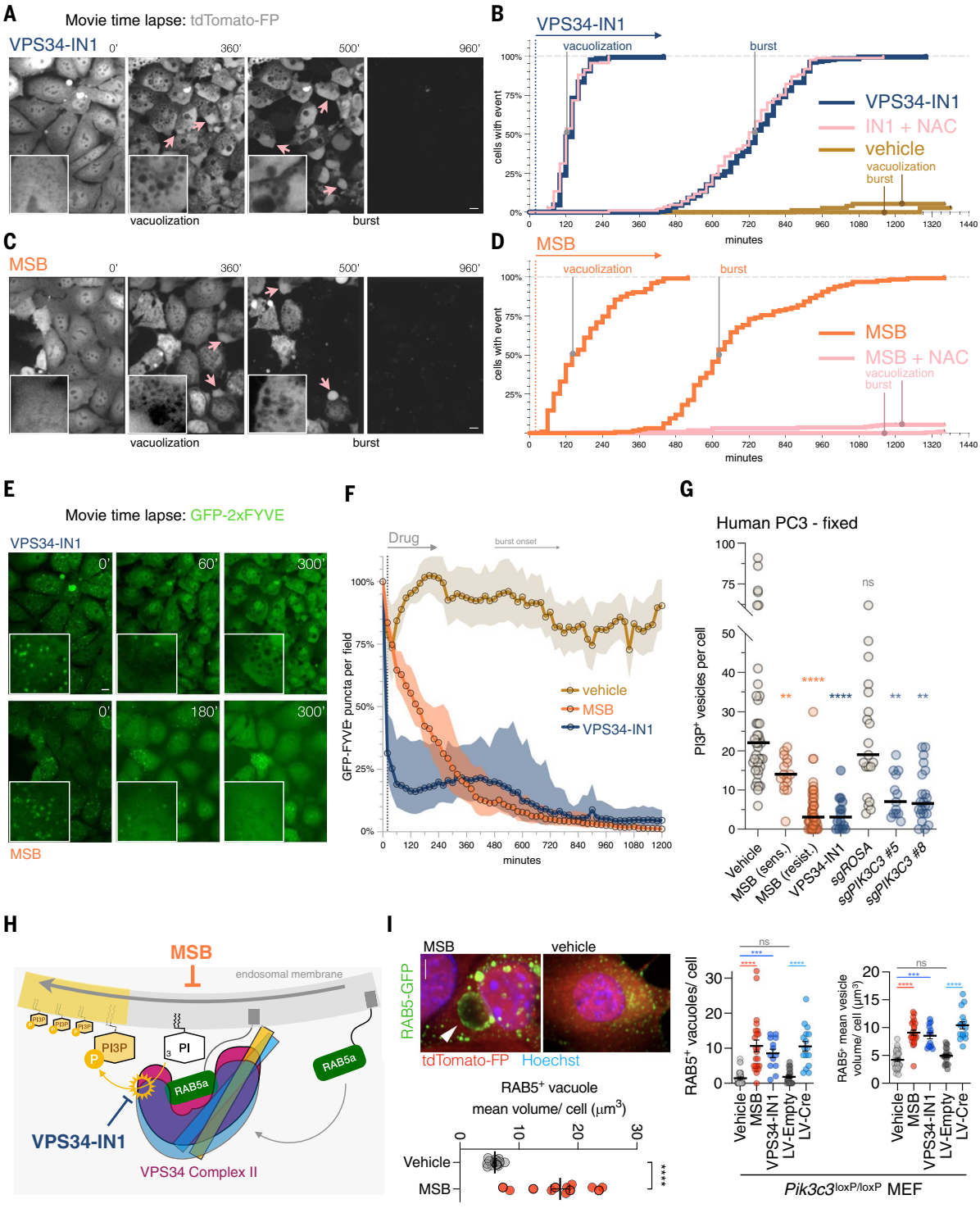

Fig. 4. VPS34 is a functional target of menadione. (**A**) Cell death analysis using EC_{100} dose of VPS34-IN1. Still images from time-lapse (20-min interval) recording of treated EpCaP cells at indicated time points. Arrows point to cell blebbing events in the field of view. Scale bar, 10 μm; inset box width, 20 μm. Please see associated movies S1 to S3. (**B**) Kaplan-Meier event analysis for VPS34-IN1 (40 μM) (n = 177 cells), VPS34-IN1 (40 μM) + NAC (500 μM) (n = 84 cells), and vehicle (n = 74 cells), scoring for (i) onset of vacuolization, as defined by time of appearance of cytoplasmic vesicles ≥3-μm diameter and (ii) burst time as scored by between-frame depletion of cytosolic tdTomato, indicating PM rupture (movies S1 to S3). P values were calculated using log-rank (Mantel-Cox) test: VPS34-IN1 versus VPS34-IN1+NAC (vacuolization: P = 0.5912; burst: P = 0.3036) and VPS34-IN1 versus vehicle (vacuolization: P < 0.0001; burst: P < 0.0001). (**C**) Cell death analysis recorded and labeled as in (A), but using EC_{100} dose of MSB. Scale bar, 10 μm; inset box width, 20 μm. Please see associated movies S4 and S5. (**D**) Kaplan-Meier event analysis for MSB (30 μM) (n = 127 cells) and MSB (30 μM) + NAC (500 μM) (n = 200 cells), scoring for (i) onset of vacuolization and (ii) burst time, as described in (B). P values were calculated using log-rank (Mantel-Cox) test: MSB versus MSB+NAC (vacuolization: P < 0.0001; burst: P < 0.0001) and MSB versus vehicle (vacuolization: P < 0.0001; burst: P < 0.0001). (**E**) Still images of the PI(3)P early endosome marker GFP-2xFYVE in time-lapse recordings from (A) and (C) with indicated treatments and times. Scale bar, 10 μm; inset box width, 20 μm. Please see associated movies S6 to S9. (**F**) Quantification of 2XGFP-FYVE puncta from time-lapse experiments shown in (A) to (E) for vehicle, MSB, and VPS34-IN1 treatment over time. Note that the marked reduction in both treatment conditions occurs before cell burst (before 480 min), as determined in (B) and (D). (**G**) Number of PI(3)P-positive vesicles in PC3-Cas9 cells fixed after 4 hours of treatment with indicated small molecules or expression of indicated sgRNAs (vehicle n = 40, MSB-low, 15 μM, n = 15, MSB-high, 25 μM, n = 51, VPS34-IN1, 10 μM, n = 14, *sgROSA* n = 21, *sgPIK3C3* no. 5 n = 13, *sgPIK3C3* no. 8 n = 22). Data are means ± SEMs. P values were calculated using one-way ANOVA. ns, not significant; **P < 0.01; ****P < 0.0001. (**H**) Cartoon for RAB5-mediated recruitment of VPS34 complex II to an endosomal membrane and its suppression by the

kinase inhibitor VPS34-IN1 and pro-oxidant MSB. (**I**) (Left top) Confocal images of EpCaP cells stably expressing tdTomato and transiently expressing RAB5-GFP after 4 hours of treatment with vehicle or MSB (15 μM). Scale bar, 5 μm. (Left bottom) Quantification of mean RAB5-GFP–positive vesicle volume per cell after vehicle (n = 14) or MSB (15 μM, n = 12) treatment. Data are means ± SEMs. P values were calculated using two-tailed unpaired Student's t test. ****P < 0.0001. (Right) Quantification of RAB5-mRFP–positive vacuoles per cell in VPS34 (*Pik3c3*$^{loxP/loxP}$) conditional KO-MEF after vehicle (n = 33), MSB (20 μM, n = 23), VPS34-IN1 (10 μM, n = 13) treatment, control (n = 22), or Cre-mediated kinase ablation (n = 16). Data are means ± SDs. P values were calculated using one-way ANOVA. ns, not significant; ***P < 0.001; ****P < 0.0001.

a fatal human disease syndrome that involves this kinase, when administered orally as we did in the PC trial. X-linked myotubular myopathy (XLMTM, OMIM no. 310400) is a heritable fatal disease in boys caused by mutation of the *MTM1* gene on chromosome X. Because MTM1 phosphatase is the direct antagonist of PI 3-kinase VPS34 (Fig. 3A), these patients suffer from unopposed PI(3)P production. This has been successfully tested in patient-derived cells (*51*).

The *Mtm1* knockout (KO) mice fully recapitulate the most severe XLMTM phenotype, lethality in infant boys (*52*, *53*). As shown (Fig. 5D), *Mtm1*-deficient male mice (*Mtm1*$^{KO/Y}$, aka *Mtm1*-KO) succumb to the disease at a median of 1 month of age owing to extensive failure of muscle buildup, as previously described (*52*). By contrast, giving MSB in drinking water significantly (P < 0.0001) expanded overall survival to a median of 62 days (Fig. 5D; see also the separate second trial below). Notably, MSB was administered as in the cancer trial (Fig. 1)—in drinking water and at the same concentration. As previously (*54*), enrollment and treatment of pups was started after weaning at 21 days of age (fig. S13A), when KO males already manifested disease symptoms (fig. S13B, WT versus KO). We confirmed that treatment decreased GSH/GSSG ratios in *Mtm1*$^{KO/Y}$ mice (fig. S13A). Body weight analysis of the entire trial (Fig. 5E) showed significantly (P < 0.0001) more weight gain in MSB-treated *Mtm1*$^{KO/Y}$ mice compared with this genotype on water, despite indistinguishable weights at enrollment day 21 (Fig. 5E, right panel; KO^{water} versus KO^{MSB}). In agreement, body images of three sets of littermates on the four treatment arms indicated that MSB-treated KO animals were larger than their KO littermates lacking MSB treatment (Fig. 5F and fig. S13C).

Histological analysis of untreated *Mtm1*$^{KO/Y}$ tibialis anterior (TA) muscles showed the previously reported myofiber hypotrophy and organelle mislocalization (*52*, *55*) (Fig. 5G) and the shift toward smaller fiber peak diameters compared with WT muscles (Fig. 5H). Upon MSB treatment, TA muscle fiber size was increased in *Mtm1*$^{KO/Y}$ mice compared with the untreated KO animals, which exhibited a higher fiber number with a small diameter (<35 μm) and a lower number of fibers with a large diameter (>35 μm; Fig. 5H). The hallmark mispositioning of nuclei (*52*) was observed in 4% of *Mtm1*$^{KO/Y}$ fibers and decreased to 2.4% in the MSB-treated KO mice (Fig. 5H). Abnormal cell-peripheral mitochondria [revealed by succinate dehydrogenase (SDH) and NADH staining; Fig. 5, H and I, and fig. S13D] was seen in 94% of untreated and decreased to 27% in MSB-treated *Mtm1*$^{KO/Y}$ mice. Thus, MSB treatment of *Mtm1*$^{KO/Y}$ mice improved several histopathological defects in TA muscle fiber. Muscle ultrastructure analysis by TEM confirmed *Mtm1* KO phenotypes (Fig. 5J): disorganized sarcomeres with misaligned Z-disks, undetectable M-line, and absence of mitochondria between myofibers. Although T-tubules are observed in untreated *Mtm1*$^{KO/Y}$ mice, triads were not. In MSB-treated *Mtm1*$^{KO/Y}$ mice, sarcomere alignment was ameliorated and mitochondria localized between myofibers, similar to WT muscle. T-tubules were also visible, but triads were not restored. Overall, muscle histology and myofiber ultrastructure were improved after MSB administration in *Mtm1*$^{KO/Y}$ mice.

Open-field cage monitoring (fig. S13, E and F) revealed that MSB improved active time, distance traveled, and median speed, but the number of rears in *Mtm1*$^{KO/Y}$ mice was not significantly different from WT only upon MSB treatment. As expected, there was no significant difference in exploratory pattern (fig. S13G). To study onset of clinical parameters in greater detail, we carried out a second trial (fig. S13H) and found that MSB treatment significantly delayed the onset of hindlimb paralysis (P < 0.001) (fig. S13I). Finally, we used the clinical score method to assess disease progression (*54*) and found a significant (P < 0.01) improvement for the *Mtm1*$^{KO/Y}$ cohort treated with MSB compared with water (fig. S13J). Taken together, our data suggested that MSB-mediated targeting of PI 3-kinase VPS34 can be used toward effective suppression of this debilitating genetic disease in mice.

Discussion

Ample evidence exists for the tumor- and metastasis-promoting role of dietary antioxidants (*2*, *3*, *56*–*58*). But it has remained ill-defined whether, vice versa, pro-oxidants can suppress cancer. We have found that dietary administration of the pro-oxidant vitamin K precursor MSB suppresses PC progression. We also show that menadione triggers an oxidative cell death by antagonizing the primordial class III PI 3-kinase VPS34, thus blocking endosomal sorting. This suggests a therapeutic opportunity, given the evidence of PC promotion by dietary antioxidants (*2*, *3*).

There is an emerging picture of how various oxidative and ROS-inducing interventions affect core cellular processes selectively, instead of broadly. Compartments and localization play a central role in specificity: Membrane lipids are the sites for ferroptosis induction and mitochondria for ETC inhibitors, and irradiation or chemotherapy can oxidize DNA in the cell nucleus (*9*, *29*, *59*–*68*).

In this work, we discovered a type of cell death controlled by oxidative depletion of PI(3)P, the token of endosomal identity. This suggests that endosomal progression is under a redox checkpoint. This checkpoint monitors the redox state of key cysteines on endosomal PI 3-kinase VPS34, licensing it to generate the EE compartment by marking it with PI(3)P.

We propose to name this new modality triaptosis, for cell death by depletion of 3-(Greek: Tría)-phosphoinositide. Upstream, early endosomes are the fusion hub for the multiple incoming clathrin-dependent and -independent endocytic vesicles. Downstream, they are the dispatching hub that guides proteins, cargo, and membranes toward either the late endo-lysosomal compartments or back toward the cell surface (*38*) by virtue of the coincident detection of RAB5 and PI(3)P. In triaptosis, loss of PI(3)P effectively deidentifies endosomes, thus disabling their downstream sorting, while incoming vesicles continue to fuse into these bloating structures.

This prompts the general question why an ancestral protein complex such as class III PI 3-kinase VPS34 and a cell-essential process such as endocytosis evolved to be under redox control. We speculate that iron metabolism may represent a prototypical case for this checkpoint. Iron is an essential nutrient that is taken up by receptor-mediated endocytosis and released through the endo-lysosomal system. Iron is then effectively liganded and stored, but there also exists an unliganded "labile" iron pool that is toxic to cells because it generates hydroxyl radicals from H_2O_2 through the Fenton reaction (*67*). Hence, it makes sense for cells to limit iron uptake and endocytosis when under oxidative stress. Suppression of iron and/or transferrin receptor uptake and recycling and also lysosomal processing have been observed after menadione treatment several decades ago (*69*), entirely consistent with our finding of PI 3-kinase VPS34 suppression by this oxidant.

Clathrin-mediated endocytosis (CME) is the major route of nutrient uptake and PM receptor regulation. Clathrin-independent endocytosis

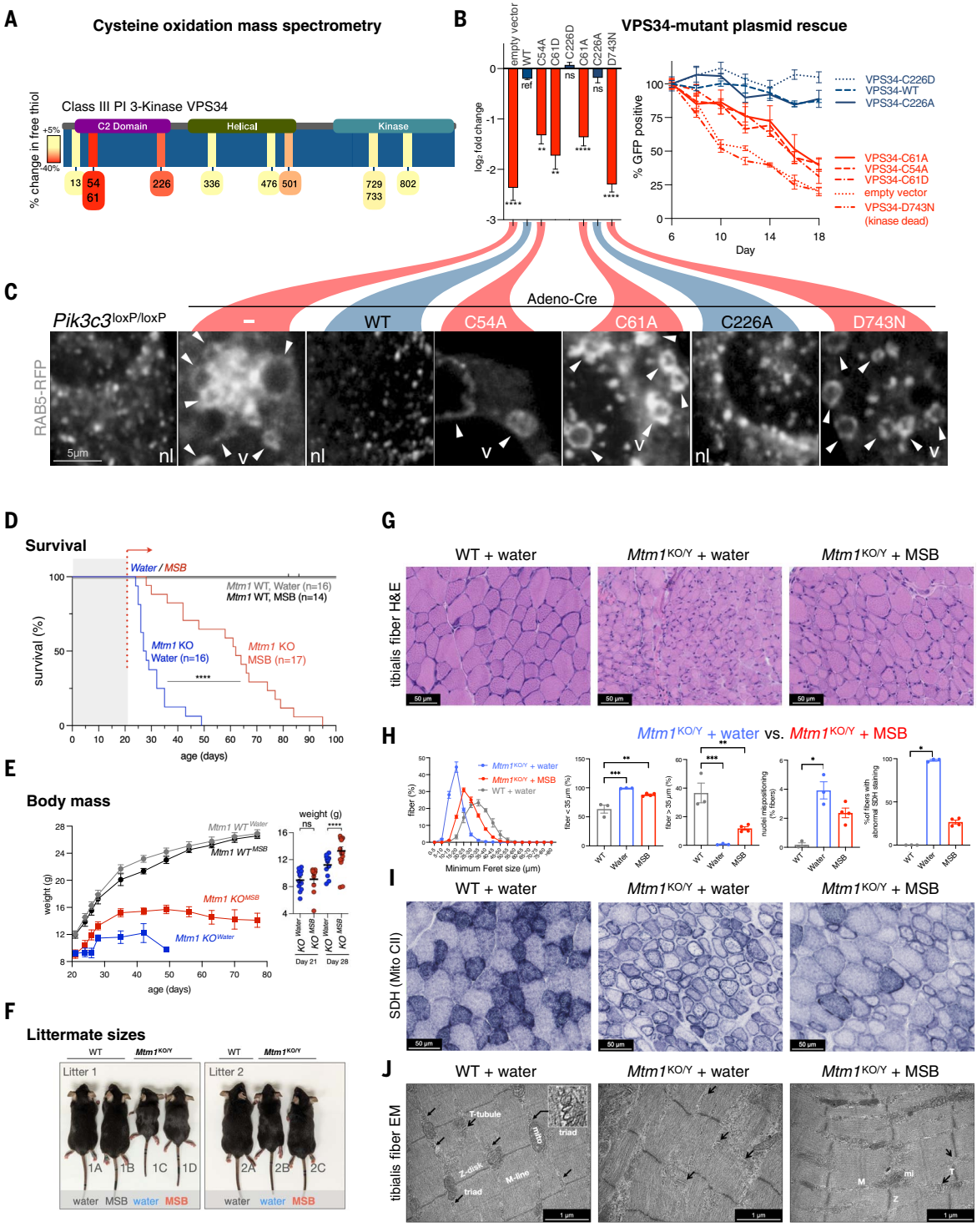

Fig. 5. Dietary menadione extends life span in a myotubular myopathy model. (**A**) (Top) Domain architecture of human class III PI 3-kinase VPS34. (Bottom) Heatmap representation of percent depletion in free thiol status of VPS34 cysteines in MSB-treated cells compared with vehicle. (**B**) (Left) Log_2 fold change in relative abundance of GFP-positive *Pik3c3*$^{\Delta/\Delta}$ cells, expressing the indicated VPS34 mutants, 18 days after Cre infection (n = 3 each). (Right) Competition-based proliferation assay in Cre and GFP-expressing *Pik3c3*$^{loxP/loxP}$ MEFs expressing the indicated VPS34 mutants. Percent GFP-positive cells, normalized to day 6 after Cre.GFP infection, are measured over time. Data are means ± SEMs. P values were calculated using one-way ANOVA. ns, not significant; $^{**}P < 0.01$; $^{****}P < 0.0001$. (**C**) Confocal images of *Pik3c3*$^{loxP/loxP}$ MEFs stably expressing RAB5-mRFP (gray) and the indicated VPS34 mutants, 10 days after adeno-empty or Cre infection. Arrowheads point to RAB5 coated endocytic vacuoles ("v"). "nl" indicates normal RAB5-positive early endocytic vesicles. Scale bar, 5 μm. (**D**) Kaplan-Meier survival curves for *Mtm1* WT and KO male mice, enrolled on the day of weaning to receive regular drinking water or MSB dissolved in the drinking water (*Mtm1* WT, water n = 16; *Mtm1* WT, MSB n = 14; *Mtm1* KO, water n = 16; *Mtm1* KO, MSB n = 17). P value was calculated by log-rank (Mantel-Cox) test. $^{****}P < 0.0001$. (**E**) Body mass of *Mtm1* WT and KO male mice from trial shown in (D): *Mtm1* WT, water n = 15; *Mtm1* WT, MSB n = 13; *Mtm1* KO, water n = 16; *Mtm1* KO, MSB n = 17. P value was calculated using two-tailed unpaired Student's t test. $^{**}P < 0.01$. (**F**) Photographs of untreated and treated *Mtm1* WT and KO male littermates from 2 litters (36-days-old), showing observed differences in size between genotypes and treatment groups. (**G**) Representative images of H&E staining in TA muscle sections of *Mtm1* WT and KO mice from the indicated trial arms. Scale bar, 50 μm. (**H**) (Left) Minimum Feret diameter (MinFeret) distribution of TA fibers in *Mtm1* WT and KO male mice from the indicated treatment arms. (Middle) Frequency of TA fibers with MinFeret diameter lower than 35 μm and higher than 35 μm, respectively. (Right) Fraction of fibers with mislocalized nuclei and abnormal SDH staining. P values were calculated using one-way ANOVA. ns, not significant; $^{*}P < 0.05$; $^{**}P < 0.01$; $^{***}P < 0.01$; $^{****}P < 0.0001$. (**I**) Representative images of SDH activity in TA muscle sections of *Mtm1* WT and KO mice from the indicated trial arms. Scale bar, 50 μm. (**J**) Representative images depicting TA ultrastructure by TEM, from untreated or MSB treated *Mtm1* WT and KO mice. Magnification of a triad is shown in TA of *Mtm1* WT mice. "mito" or "mi" indicates mitochondria. Scale bar, 1 μm.

(CIE) routes also exist, and they are key in cancer: Mutant Ras boosts macropinocytosis through class I PI 3-kinase (*70*, *71*). After PTEN loss, unchecked action of class I PI 3-kinase promotes macropinocytosis and FEME, another type of CIE. Endophilin and drivers of macropinocytosis were among the top hits in the sensitizing screen (Fig. 3A), consistent with the ability of CIE pathways to support fitness of the PC cells under low-dose MSB oxidative stress. This is because by triggering the proposed endosomal redox checkpoint, PI(3)P levels drop, and VPS34-independent sources of PI(3)P become critical. This requires an elaborate and inefficient enzymatic detour that depends on class I and class II PI 3-kinases and a multitude of PIP metabolizing enzymes (*38*, *72*). Thus, it is entirely expected that these alternatives cannot prevent triaptosis upon class III PI 3-kinase VPS34 inactivation, because 70 to 80% of the cell's PI(3)P pool is produced in a single step by this enzyme (*38*, *73*, *74*). By contrast, however, thiol reducing power completely rescued triaptosis, which suggests that cells with sufficient reducing reserves can overcome this stress. This may be the basis for our observed therapeutic window.

The generation of mouse models for XLMTM and related centronuclear myopathy syndromes has led to several successful preclinical trials, and this has spawned a number of clinical trials to help affected patients (*75*). Problems associated with human gene therapy (*76*) have unfortunately stymied the translation of highly successful gene therapy in mice and dogs that reconstituted the *Mtm1* gene. At the same time, new human trials have been started based on the unexpected preclinical success with drug repurposing: It was shown that tamoxifen can be used to strongly ameliorate the disease in *Mtm1*-KO mice (*54*, *77*). Moreover, it has been shown that loss of class II PI 3-kinase (*Pik3c2b*) reverses the lethal *Mtm1*-KO phenotype, whereas the pan–PI 3-kinase inhibitor wortmannin extends survival in these mice (*51*, *78*–*80*). It will be important to see how progress with the therapeutic windows of PI 3-kinase class II and class III inhibitors affect the design of myotubular myopathy trials. Although key points for clinical translation remain to be tested (dose-response, drug accumulation in muscle, and force generation), it is encouraging that the improvements in life span and activity may be linked to improvements in muscle histology and myofiber ultrastructure. Thus, our preclinical results based on dietary menadione have the potential to expand the toolbox for therapy of XLMTM and perhaps even other centronuclear myopathies more broadly.

Taken together, we discovered the opportunity for suppressing class III PI 3-kinase VPS34 with the provitamin menadione and its consequence, the distinct cell death by triaptosis. We suggest that these findings may offer much needed lines of attack in multiple human disease settings.

Materials and methods summary

Generation of RapidCaP mice

Pten$^{loxP/loxP}$;*Trp53*$^{loxP/loxP}$ transgenic mice were used in this study. All protocols for mouse experiments were in accordance with institutional guidelines and were approved by the Institutional Animal Care and Use Committee (IACUC). *Pten*$^{loxP/loxP}$;*Trp53*$^{loxP/loxP}$ transgenic mice were generated by crossing *Pten*$^{loxP/loxP}$ mice with *Trp53*$^{loxP/loxP}$ mice. Eight-week-old *Pten*$^{loxP/loxP}$;*Trp53*$^{loxP/loxP}$ transgenic male mice were used for RapidCaP surgery. The detailed method has been described previously (*4*, *5*, *81*). After exposure to anesthesia (isoflurane, 2%), the lower half of the abdomen was shaved, and the mouse was placed in a sterile surgical hood. The mouse was constantly exposed to isoflurane through a nose cone for the entire duration of the 10-min surgery. The shaved region was cleaned with betadine, followed by ethanol three times. A 0.5-inch incision in both the skin and peritoneum was made along the lower abdomen, to the right of the midline, to allow the right anterior prostate to be exposed. The right anterior prostate is removed from the body and placed on a sterile drape. Then, 20 μl of concentrated Luc.Cre virus (Addgene plasmid no. 20905, 2.5×10^7 transduction units per ml), purchased from the University of Iowa's Viral Vector Core, was injected into the right anterior prostate. The incision was then sutured with absorbable sutures and the skin stapled shut using two to three stainless steel EZ Clip wound closures. Animals were observed for complete recovery from anesthesia and warmed under a heating lamp to regain the ability to maintain sternal recumbence and given DietGel.

Generation of MTM mice

MTM heterozygous female mice (*Mtm1*$^{+/-}$) containing a targeted deletion in exon 4 of one *Mtm1* (*52*) were crossed with *Mtm1*$^{+/Y}$ males and were maintained on a C57BL/6J background for several generations, after confirmation of the genetic background using externally validated genetic monitoring single-nucleotide polymorphism (SNP) panels (MiniMUGA array, Transnetyx). For genotyping, genomic DNA was isolated using tail clips and subjected to polymerase chain reaction (PCR) analysis using the following primers: Forward: 5′-AGCACATGGGAGGTTGAG-3′. Reverse: 5′-GGCTTTAACCAAGGATTCACA-3′. The presence of WT and Mtm1δ4 alleles result in a 0.9 kb and 0.2 kb DNA fragment, respectively.

Animal trials

For trials on RapidCaP animals, mice with sustained disease as determined by 4 weeks of BLI were randomized and assigned to three cohorts receiving water control (n = 7), a dose of 0.15 mg/ml of MSB (Sigma-Aldrich, M5750) (n = 7), or a combination of 0.15 mg/ml MSB with 15 mg/ml VC (Sigma-Aldrich, A7631) (n = 8). The compounds were dissolved fresh daily in autoclaved water and provided to the mice ad libitum. Drug consumption was recorded daily (in milliliters) to ensure consistent dosing between and within cohorts. Mice were monitored weekly for weight loss as well as disease progression using BLI. At the end of the 18-week trial period, mice were humanely euthanized, and the prostates were excised and flash frozen for MS analysis. For BLI, mice were intraperitoneally (IP) injected with D-Luciferin (GoldBio, 115144-35-9) (50 mg/kg) and analyzed using an IVIS Spectrum system (Caliper Life Sciences) 10 min after IP injection. For signal quantification, Living Image was used. The two animals with Δendpoints > 3rd quartile + 1.5 × interquartile range of their respective cohort (MSB no. 8 = 1312% > 118.5; MSB & VC no. 8 = 1379% > 293.0) were defined as statistical outliers.

To determine effects on coagulation, naïve mice were dosed with increasing concentrations of MSB (0.15 mg/ml to 0.75 mg/ml). The treatment was provided ad libitum and made fresh daily. Blood coagulation was tested biweekly using the Roche CoaguChek XS device. Mice were restrained, and a small tail vein puncture was performed. Within 15 s of the tail vein puncture, 50 μl of blood was dripped on to the CoaguChek test strip, and the reading was recorded.

VC levels were determined and showed no increase in normal liver (MSB & VC: 2.05 nmol/mg, SD = 0.65 nmol/mg versus water: 2.46 nmol/mg, SD = 0.02 nmol/mg) and prostate (MSB & VC: 1.78 nmol/mg, SD = 0.29 nmol/mg versus water: 1.64 nmol/mg, SD = 0.14 nmol/mg) of three trial animals, each using the Ascorbic Acid Assay Kit (Sigma-Aldrich, MAK074-1KT).

For transplantation experiments in Nu/J male mice (JAX stock no. 002019), 100,000 RapidCaP-derived *Pten*$^{-/-}$;*Trp53*$^{-/-}$ EpCaP cells were mixed with an equal volume of Matrigel and then subcutaneously injected. The tumors were allowed to engraft and then (10 days after injection), mice were enrolled on a randomized basis to be treated with phosphate-buffered saline (PBS) or MSB (50 mg/kg). The treatment was delivered through IP injections on a daily basis. At the end of 1 week, mice were humanely euthanized, and the prostates were excised and flash frozen for MS analysis. For transplantation experiments in C57BL/6 male mice, 250,000 RapidCaP-derived *Pten*$^{-/-}$;*Trp53*$^{-/-}$ EpCaP cells were mixed with an equal volume of Matrigel and then orthotopically injected into the right anterior prostate using the surgical procedure for RapidCaP generation as described earlier. The tumors were allowed to engraft and then (10 days after injection), mice were enrolled on a randomized basis to receive regular drinking water or 0.15 mg/ml of MSB dissolved in the drinking water. The compounds were dissolved fresh in autoclaved water, three times a week, and provided to the mice ad libitum. At the end

of 10 days, mice were humanely euthanized, and the prostates were excised and flash frozen for RNA extraction.

For the MTM trials, *Mtm1* WT ($Mtm1^{WT/Y}$ or $Mtm1^{+/Y}$) and *Mtm1* KO ($Mtm1^{KO/Y}$) male mice were weaned on postnatal day 21 and randomly enrolled to receive regular drinking water or 0.15 mg/ml of MSB dissolved in the drinking water. The compounds were dissolved fresh in autoclaved water, three times a week, and provided to the mice ad libitum. $Mtm1^{KO/Y}$ animals were kept on the respective treatments until death as the endpoint. Animal weights were recorded on days 21, 24, 26, and 28 and then on a weekly basis.

For phenotypic assessment of mouse motor functions, we analyzed activity of the animals using an open-field test. Mouse mobility was tested in a 40-cm (L) by 22-cm (W) by 25-cm (H) black acrylic box. A camera was mounted above the box and connected to a PC using a USB2.0 cable for video recording. The axis of the camera was perpendicular to the box ground so that the videos showed mouse movements on the horizontal plane. On the test day, mice in their home cages were transferred to the test room at least 1 hour before the test started. Each mouse was gently loaded to the center of box ground by hand and then allowed to explore the box freely for 3 min while video recording was on. After that, the mouse was returned to its home cage and home room. The box was cleaned using 70% alcohol and paper towels between consecutive animals. Tests were done on 3 days after enrollment to a treatment condition.

The first 3 min after the mouse was loaded into the box were analyzed from video files. The (x, y) coordinates of mouse location on each frame of video recordings were determined using the python package ezTrack (*82*). The resulting coordinates were then transformed to derive displacement, $d_i = [(x_i - x_{i-1})^2 + (y_i - y_{i-1})^2]^{0.5}$ and mobility $v_i = (d_i)$ x (frame rate) for the i^{th} frame. A separate video clip of a mouse sitting at a fixed location without overt displacement by eye was used to set the threshold of movement for all other mice. Any frame with displacement above that threshold was considered as an active frame. Proportion of active time was calculated as percentage of active frames to all frames in 3 min. Total displacement was the sum of displacement in the active time.

Electron microscopy

TA muscles were fixed by immersion in 2.5% paraformaldehyde and 2.5% glutaraldehyde in 0.1 M cacodylate buffer (pH = 7.4), then washed in cacodylate buffer for 30 min. Muscles were postfixed in 1% osmium tetroxide in 0.1 M cacodylate buffer for 1 hour at 4°C and dehydrated through graded alcohol (50, 70, 90, and 100%) and propylene oxide for 30 min each. The samples were embedded in Epon 812 before semithin sections were cut at 2 μm. Ultrathin sections were cut at 70 nm (Leica Ultracut UCT) and contrasted with uranyl acetate and lead citrate. Sections were observed at 70kv with a Morgagni 268D electron microscope (FEI Electron Optics, Eindhoven, Netherlands). Images were captured digitally by Mega View III camera (Soft Imaging System). The number of T-tubules per sarcomere and T-tubule direction were measured manually.

Histology

Eight-micrometer-thick transversal cryosections of TA muscles were collected on glass slides and stained with hematoxylin and eosin (H&E) or SDH. Light microscopic images were acquired using a Nanozoomer 2HT slide scanner (Hamamatsu Photonics). Myofiber size was measured by the Cellpose segmentation algorithm on H&E sections (*83*). Images were analyzed using FIJI analysis software. Myofiber MinFeret diameter (in micrometers) and nuclei mislocalization analyses were performed on H&E images. SDH images were used for analysis of mitochondria mispositioning. Fibers with abnormal SDH staining and nuclei positioning were counted manually using the cell counter plugin in FIJI analysis software. Myofiber size, abnormal SDH staining, and nuclei mislocalization were determined from fibers of the whole muscle section.

Single-nucleus processing for whole-genome sequencing

For single-cell genomics, we used the single-nucleus sequencing (SNS) approach. Animals were euthanized using CO_2 exposure, tissues of interest were harvested and imaged on the Xenogen or IVIS after application of luciferin ex vivo. Regions with BLI signal were then dissected and flash frozen. To isolate cells from the bone, the femur was flushed with PBS, collected, and BLI imaged to confirm presence of mutant cells followed by staining with CD45 antibody and sorting of the CD45-negative population by FACS. Nuclei were isolated for SNS from frozen and FACS-sorted samples using the previously published protocol (*15*). Samples were lysed in the NST-DAPI buffer (*15*), [800 ml of NST (146 mM NaCl, 10 mM Tris base at pH 7.8, 1 mM $CaCl_2$, 21 mM $MgCl_2$, 0.05% BSA, 0.2% NP-40)] 200 ml of 106 mM $MgCl_2$, 10 ml of 500 mM EDTA at pH 8.0, and 10 mg of DAPI (Cell Signaling Technology, 4083S). Nuclei were prepared by gently centrifuging the cell lysis solution at 1000 rpm for 5 min to pellet them followed by removal of supernatant and addition of 1 ml of NST-DAPI buffer to the cell pellet. Suspensions of nuclei were filtered through a 25-mm cell strainer before flow sorting. Single nuclei were sorted by FACS using the BD Biosystems SORP flow cytometer, and single nuclei were deposited into individual wells of a 96-well plate.

For whole-genome amplification (WGA) and Illumina library construction, the Seqplex DNA amplification kit (Sigma-Aldrich, SEQXE-50RXN) was used according to the manufacturer's instructions. Before library preparation the Seqplex primers were first removed enzymatically. One microgram of WGA product was then end-repaired, A-tailed, and ligated to TruSeq adapters (illumina). The ligated DNA was purified using AMPure XP beads (Beckman Coulter) then pooled, amplified, and quantified for sequencing using a Bioanalyzer 2100 (Agilent). The pools were sequenced on the Illumina NextSeq 500 instrument using single-read 76 bp.

REFERENCES AND NOTES

1. R. L. Siegel, A. N. Giaquinto, A. Jemal, Cancer statistics, 2024. *CA Cancer J. Clin.* **74**, 12–49 (2024). doi: 10.3322/caac.21820; pmid: 38230766
2. S. M. Lippman *et al.*, Effect of selenium and vitamin E on risk of prostate cancer and other cancers: The Selenium and Vitamin E Cancer Prevention Trial (SELECT). *JAMA* **301**, 39–51 (2009). doi: 10.1001/jama.2008.864; pmid: 19066370
3. E. A. Klein *et al.*, Vitamin E and the risk of prostate cancer: The Selenium and Vitamin E Cancer Prevention Trial (SELECT). *JAMA* **306**, 1549–1556 (2011). doi: 10.1001/jama.2011.1437; pmid: 21990298
4. H. Cho *et al.*, RapidCaP, a novel GEM model for metastatic prostate cancer analysis and therapy, reveals myc as a driver of *Pten*-mutant metastasis. *Cancer Discov.* **4**, 318–333 (2014). doi: 10.1158/2159-8290.CD-13-0346; pmid: 24444712
5. D. G. Nowak *et al.*, MYC Drives *Pten/Trp53*-Deficient Proliferation and Metastasis due to IL6 Secretion and AKT Suppression via PHLPP2. *Cancer Discov.* **5**, 636–651 (2015). doi: 10.1158/2159-8290.CD-14-1113; pmid: 25829425
6. J. Taranda *et al.*, Combined whole-organ imaging at single-cell resolution and immunohistochemical analysis of prostate cancer and its liver and brain metastases. *Cell Rep.* **37**, 110027 (2021). doi: 10.1016/j.celrep.2021.110027; pmid: 34788609
7. W. J. Liang, D. Johnson, S. M. Jarvis, Vitamin C transport systems of mammalian cells. *Mol. Membr. Biol.* **18**, 87–95 (2001). doi: 10.1080/09687680110033774; pmid: 11396616
8. K. R. Keshari *et al.*, Hyperpolarized ^{13}C dehydroascorbate as an endogenous redox sensor for in vivo metabolic imaging. *Proc. Natl. Acad. Sci. U.S.A.* **108**, 18606–18611 (2011). doi: 10.1073/pnas.1106920108; pmid: 22042839
9. J. Yun *et al.*, Vitamin C selectively kills *KRAS* and *BRAF* mutant colorectal cancer cells by targeting GAPDH. *Science* **350**, 1391–1396 (2015). doi: 10.1126/science.aaa5004; pmid: 26541605
10. A. Magrì *et al.*, High-dose vitamin C enhances cancer immunotherapy. *Sci. Transl. Med.* **12**, eaay8707 (2020). doi: 10.1126/scitranslmed.aay8707; pmid: 32102933
11. K. R. Keshari *et al.*, Hyperpolarized [1-^{13}C]dehydroascorbate MR spectroscopy in a murine model of prostate cancer: Comparison with ^{18}F-FDG PET. *J. Nucl. Med.* **54**, 922–928 (2013). doi: 10.2967/jnumed.112.115402; pmid: 23575993
12. J. Verrax *et al.*, Enhancement of quinone redox cycling by ascorbate induces a caspase-3 independent cell death in human leukaemia cells. An *in vitro* comparative study. *Free Radic. Res.* **39**, 649–657 (2005). doi: 10.1080/10715760500097906; pmid: 16036343
13. B. S. Taylor *et al.*, Integrative genomic profiling of human prostate cancer. *Cancer Cell* **18**, 11–22 (2010). doi: 10.1016/j.ccr.2010.05.026; pmid: 20579941
14. J. Armenia *et al.*, The long tail of oncogenic drivers in prostate cancer. *Nat. Genet.* **50**, 645–651 (2018). doi: 10.1038/s41588-018-0078-z; pmid: 29610475
15. J. Alexander *et al.*, Utility of Single-Cell Genomics in Diagnostic Evaluation of Prostate Cancer. *Cancer Res.* **78**, 348–358 (2018). doi: 10.1158/0008-5472.CAN-17-1138; pmid: 29180472
16. B. Lim, Y. Lin, N. Navin, Advancing Cancer Research and Medicine with Single-Cell Genomics. *Cancer Cell* **37**, 456–470 (2020). doi: 10.1016/j.ccell.2020.03.008; pmid: 32289270
17. F. Sanchez-Vega *et al.*, Oncogenic Signaling Pathways in The Cancer Genome Atlas. *Cell* **173**, 321–337.e10 (2018). doi: 10.1016/j.cell.2018.03.035; pmid: 29625050

18. C. Tonelli, I. I. C. Chio, D. A. Tuveson, Transcriptional Regulation by Nrf2. *Antioxid. Redox Signal.* **29**, 1727–1745 (2018). doi: 10.1089/ars.2017.7342; pmid: 28899199
19. R. M. Meyers *et al*., Computational correction of copy number effect improves specificity of CRISPR-Cas9 essentiality screens in cancer cells. *Nat. Genet.* **49**, 1779–1784 (2017). doi: 10.1038/ng.3984; pmid: 29083409
20. J. V. Gerasimenko *et al*., Menadione-induced apoptosis: Roles of cytosolic Ca^{2+} elevations and the mitochondrial permeability transition pore. *J. Cell Sci.* **115**, 485–497 (2002). doi: 10.1242/jcs.115.3.485; pmid: 11861756
21. G. Loor *et al*., Menadione triggers cell death through ROS-dependent mechanisms involving PARP activation without requiring apoptosis. *Free Radic. Biol. Med.* **49**, 1925–1936 (2010). doi: 10.1016/j.freeradbiomed.2010.09.021; pmid: 20937380
22. J. A. Armstrong *et al*., Oxidative stress alters mitochondrial bioenergetics and modifies pancreatic cell death independently of cyclophilin D, resulting in an apoptosis-to-necrosis shift. *J. Biol. Chem.* **293**, 8032–8047 (2018). doi: 10.1074/jbc.RA118.003200; pmid: 29626097
23. A. Ben-Shem, F. Frolow, N. Nelson, Crystal structure of plant photosystem I. *Nature* **426**, 630–635 (2003). doi: 10.1038/nature02200; pmid: 14668855
24. D. E. Green, A. Tzagoloff, The mitochondrial electron transfer chain. *Arch. Biochem. Biophys.* **116**, 293–304 (1966). doi: 10.1016/0003-9861(66)90036-1; pmid: 4289862
25. A. Kröger, M. Klingenberg, The kinetics of the redox reactions of ubiquinone related to the electron-transport activity in the respiratory chain. *Eur. J. Biochem.* **34**, 358–368 (1973). doi: 10.1111/j.1432-1033.1973.tb02767.x; pmid: 4351161
26. M. Vos *et al*., Vitamin K_2 is a mitochondrial electron carrier that rescues pink1 deficiency. *Science* **336**, 1306–1310 (2012). doi: 10.1126/science.1218632; pmid: 22582012
27. A. Naguib *et al*., Mitochondrial Complex I Inhibitors Expose a Vulnerability for Selective Killing of *Pten*-Null Cells. *Cell Rep.* **23**, 58–67 (2018). doi: 10.1016/j.celrep.2018.03.032; pmid: 29617673
28. W. W. Wheaton *et al*., Metformin inhibits mitochondrial complex I of cancer cells to reduce tumorigenesis. *eLife* **3**, e02242 (2014). doi: 10.7554/eLife.02242; pmid: 24843020
29. S. J. Dixon *et al*., Ferroptosis: An iron-dependent form of nonapoptotic cell death. *Cell* **149**, 1060–1072 (2012). doi: 10.1016/j.cell.2012.03.042; pmid: 22632970
30. W. S. Yang, B. R. Stockwell, Ferroptosis: Death by Lipid Peroxidation. *Trends Cell Biol.* **26**, 165–176 (2016). doi: 10.1016/j.tcb.2015.10.014; pmid: 26653790
31. A. J. Wolpaw *et al*., Modulatory profiling identifies mechanisms of small molecule-induced cell death. *Proc. Natl. Acad. Sci. U.S.A.* **108**, E771–E780 (2011). doi: 10.1073/pnas.1106149108; pmid: 21896738
32. K. Shimada *et al*., Global survey of cell death mechanisms reveals metabolic regulation of ferroptosis. *Nat. Chem. Biol.* **12**, 497–503 (2016). doi: 10.1038/nchembio.2079; pmid: 27159577
33. L. B. Sullivan *et al*., Supporting Aspartate Biosynthesis Is an Essential Function of Respiration in Proliferating Cells. *Cell* **162**, 552–563 (2015). doi: 10.1016/j.cell.2015.07.017; pmid: 26232225
34. L. Galluzzi *et al*., Molecular mechanisms of cell death: Recommendations of the Nomenclature Committee on Cell Death 2018. *Cell Death Differ.* **25**, 486–541 (2018). doi: 10.1038/s41418-017-0012-4; pmid: 29362479
35. E. Boucrot *et al*., Endophilin marks and controls a clathrin-independent endocytic pathway. *Nature* **517**, 460–465 (2015). doi: 10.1038/nature14067; pmid: 25517094
36. S. Watanabe, E. Boucrot, Fast and ultrafast endocytosis. *Curr. Opin. Cell Biol.* **47**, 64–71 (2017). doi: 10.1016/j.ceb.2017.02.013; pmid: 28391090
37. J. M. Backer, The intricate regulation and complex functions of the Class III phosphoinositide 3-kinase Vps34. *Biochem. J.* **473**, 2251–2271 (2016). doi: 10.1042/BCJ20160170; pmid: 27470591
38. Y. Posor, W. Jang, V. Haucke, Phosphoinositides as membrane organizers. *Nat. Rev. Mol. Cell Biol.* **23**, 797–816 (2022). doi: 10.1038/s41580-022-00490-x; pmid: 35589852
39. F. Blondeau *et al*., Myotubularin, a phosphatase deficient in myotubular myopathy, acts on phosphatidylinositol 3-kinase and phosphatidylinositol 3-phosphate pathway. *Hum. Mol. Genet.* **9**, 2223–2229 (2000). doi: 10.1093/oxfordjournals.hmg.a018913; pmid: 11001925
40. C. Cao, J. Laporte, J. M. Backer, A. Wandinger-Ness, M. P. Stein, Myotubularin lipid phosphatase binds the hVPS15/hVPS34 lipid kinase complex on endosomes. *Traffic* **8**, 1052–1067 (2007). doi: 10.1111/j.1600-0854.2007.00586.x; pmid: 17651088
41. R. Bago *et al*., Characterization of VPS34-IN1, a selective inhibitor of Vps34, reveals that the phosphatidylinositol 3-phosphate-binding SGK3 protein kinase is a downstream target of class III phosphoinositide 3-kinase. *Biochem. J.* **463**, 413–427 (2014). doi: 10.1042/BJ20140889; pmid: 25177796
42. N. Jaber *et al*., Class III PI3K Vps34 plays an essential role in autophagy and in heart and liver function. *Proc. Natl. Acad. Sci. U.S.A.* **109**, 2003–2008 (2012). doi: 10.1073/pnas.1112848109; pmid: 22308354
43. F. Law *et al*., The VPS34 PI3K negatively regulates RAB-5 during endosome maturation. *J. Cell Sci.* **130**, 2007–2017 (2017). doi: 10.1242/jcs.194746; pmid: 28455411
44. A. Naguib *et al*., PTEN functions by recruitment to cytoplasmic vesicles. *Mol. Cell* **58**, 255–268 (2015). doi: 10.1016/j.molcel.2015.03.011; pmid: 25866245
45. D. J. Gillooly *et al*., Localization of phosphatidylinositol 3-phosphate in yeast and mammalian cells. *EMBO J.* **19**, 4577–4588 (2000). doi: 10.1093/emboj/19.17.4577 pmid: 10970851
46. S. Christoforidis *et al*., Phosphatidylinositol-3-OH kinases are Rab5 effectors. *Nat. Cell Biol.* **1**, 249–252 (1999). doi: 10.1038/12075; pmid: 10559924
47. K. Rostislavleva *et al*., Structure and flexibility of the endosomal Vps34 complex reveals the basis of its function on membranes. *Science* **350**, aac7365 (2015). doi: 10.1126/science.aac7365; pmid: 26450213
48. Y. Ohashi, S. Tremel, R. L. Williams, VPS34 complexes from a structural perspective. *J. Lipid Res.* **60**, 229–241 (2019). doi: 10.1194/jlr.R089490; pmid: 30397185
49. S. Miller *et al*., Shaping development of autophagy inhibitors with the structure of the lipid kinase Vps34. *Science* **327**, 1638–1642 (2010). doi: 10.1126/science.1184429; pmid: 20339072
50. S. Tremel *et al*., Structural basis for VPS34 kinase activation by Rab1 and Rab5 on membranes. *Nat. Commun.* **12**, 1564 (2021). doi: 10.1038/s41467-021-21695-2; pmid: 33692360
51. K. Ketel *et al*., A phosphoinositide conversion mechanism for exit from endosomes. *Nature* **529**, 408–412 (2016). doi: 10.1038/nature16516; pmid: 26760201
52. A. Buj-Bello *et al*., The lipid phosphatase myotubularin is essential for skeletal muscle maintenance but not for myogenesis in mice. *Proc. Natl. Acad. Sci. U.S.A.* **99**, 15060–15065 (2002). doi: 10.1073/pnas.212498399; pmid: 12391329
53. E. Sarikaya *et al*., Natural history of a mouse model of X-linked myotubular myopathy. *Dis. Model. Mech.* **15**, dmm049342 (2022). doi: 10.1242/dmm.049342; pmid: 35694952
54. E. Gayi *et al*., Tamoxifen prolongs survival and alleviates symptoms in mice with fatal X-linked myotubular myopathy. *Nat. Commun.* **9**, 4848 (2018). doi: 10.1038/s41467-018-07058-4; pmid: 30451843
55. V. M. Lionello *et al*., Amphiphysin 2 modulation rescues myotubular myopathy and prevents focal adhesion defects in mice. *Sci. Transl. Med.* **11**, eaav1866 (2019). doi: 10.1126/scitranslmed.aav1866; pmid: 30894500
56. G. M. DeNicola *et al*., Oncogene-induced Nrf2 transcription promotes ROS detoxification and tumorigenesis. *Nature* **475**, 106–109 (2011). doi: 10.1038/nature10189; pmid: 21734707
57. E. Piskounova *et al*., Oxidative stress inhibits distant metastasis by human melanoma cells. *Nature* **527**, 186–191 (2015). doi: 10.1038/nature15726; pmid: 26466563
58. C. Wiel *et al*., BACH1 Stabilization by Antioxidants Stimulates Lung Cancer Metastasis. *Cell* **178**, 330–345.e22 (2019). doi: 10.1016/j.cell.2019.06.005; pmid: 31257027
59. H. Pelicano *et al*., Inhibition of mitochondrial respiration: A novel strategy to enhance drug-induced apoptosis in human leukemia cells by a reactive oxygen species-mediated mechanism. *J. Biol. Chem.* **278**, 37832–37839 (2003). doi: 10.1074/jbc.M301546200; pmid: 12853461
60. C. C. Winterbourn, Reconciling the chemistry and biology of reactive oxygen species. *Nat. Chem. Biol.* **4**, 278–286 (2008). doi: 10.1038/nchembio.85; pmid: 18421291
61. Z. T. Schafer *et al*., Antioxidant and oncogene rescue of metabolic defects caused by loss of matrix attachment. *Nature* **461**, 109–113 (2009). doi: 10.1038/nature08268; pmid: 19693011
62. I. I. C. Chio *et al*., NRF2 Promotes Tumor Maintenance by Modulating mRNA Translation in Pancreatic Cancer. *Cell* **166**, 963–976 (2016). doi: 10.1016/j.cell.2016.06.056; pmid: 27477511
63. I. S. Harris *et al*., Deubiquitinases Maintain Protein Homeostasis and Survival of Cancer Cells upon Glutathione Depletion. *Cell Metab.* **29**, 1166–1181.e6 (2019). doi: 10.1016/j.cmet.2019.01.020; pmid: 30799286
64. H. Kong *et al*., Metabolic determinants of cellular fitness dependent on mitochondrial reactive oxygen species. *Sci. Adv.* **6**, eabb7272 (2020). doi: 10.1126/sciadv.abb7272; pmid: 33148642
65. G. Lei *et al*., The role of ferroptosis in ionizing radiation-induced cell death and tumor suppression. *Cell Res.* **30**, 146–162 (2020). doi: 10.1038/s41422-019-0263-3; pmid: 31949285
66. A. Peters, T. S. Nawrot, A. A. Baccarelli, Hallmarks of environmental insults. *Cell* **184**, 1455–1468 (2021). doi: 10.1016/j.cell.2021.01.043; pmid: 33657411
67. H. Sies *et al*., Defining roles of specific reactive oxygen species (ROS) in cell biology and physiology. *Nat. Rev. Mol. Cell Biol.* **23**, 499–515 (2022). doi: 10.1038/s41580-022-00456-z; pmid: 35190722
68. J. Zhang *et al*., Systematic identification of anticancer drug targets reveals a nucleus-to-mitochondria ROS-sensing pathway. *Cell* **186**, 2361–2379.e25 (2023). doi: 10.1016/j.cell.2023.04.026; pmid: 37192619
69. W. Malorni, F. Iosi, M. T. Santini, U. Testa, Menadione-induced oxidative stress leads to a rapid down-modulation of transferrin receptor recycling. *J. Cell Sci.* **106**, 309–318 (1993). doi: 10.1242/jcs.106.1.309; pmid: 8270633
70. C. Commisso *et al*., Macropinocytosis of protein is an amino acid supply route in Ras-transformed cells. *Nature* **497**, 633–637 (2013). doi: 10.1038/nature12138; pmid: 23665962
71. W. Palm *et al*., The Utilization of Extracellular Proteins as Nutrients Is Suppressed by mTORC1. *Cell* **162**, 259–270 (2015). doi: 10.1016/j.cell.2015.06.017; pmid: 26144316
72. M. F. Lee, L. C. Trotman, PTEN: Bridging Endocytosis and Signaling. *Cold Spring Harb. Perspect. Med.* **10**, a036103 (2020). doi: 10.1101/cshperspect.a036103; pmid: 31818848
73. K. Devereaux *et al*., Regulation of mammalian autophagy by class II and III PI 3-kinases through PI3P synthesis. *PLOS ONE* **8**, e76405 (2013). doi: 10.1371/journal.pone.0076405; pmid: 24098492
74. I. Franco *et al*., PI3K class II α controls spatially restricted endosomal PtdIns3*P* and Rab11 activation to promote primary cilium function. *Dev. Cell* **28**, 647–658 (2014). doi: 10.1016/j.devcel.2014.01.022; pmid: 24697898
75. R. Gómez-Oca, B. S. Cowling, J. Laporte, Common Pathogenic Mechanisms in Centronuclear and Myotubular Myopathies and Latest Treatment Advances. *Int. J. Mol. Sci.* **22**, 11377 (2021). doi: 10.3390/ijms222111377; pmid: 34768808
76. J. M. Wilson, "Moving Forward after Two Deaths in a Gene Therapy Trial of Myotubular Myopathy," *Genetic Engineering & Biotechnology News*, 2 July 2020; https://www.genengnews.com/insights/moving-forward-after-two-deaths-in-a-gene-therapy-trial-of-myotubular-myopathy/.
77. N. Maani *et al*., Tamoxifen therapy in a murine model of myotubular myopathy. *Nat. Commun.* **9**, 4849 (2018). doi: 10.1038/s41467-018-07057-5; pmid: 30451841
78. C. Kutchukian *et al*., Phosphatidylinositol 3-kinase inhibition restores Ca^{2+} release defects and prolongs survival in myotubularin-deficient mice. *Proc. Natl. Acad. Sci. U.S.A.* **113**, 14432–14437 (2016). doi: 10.1073/pnas.1604099113; pmid: 27911767
79. N. Sabha *et al*., PIK3C2B inhibition improves function and prolongs survival in myotubular myopathy animal models. *J. Clin. Invest.* **126**, 3613–3625 (2016). doi: 10.1172/JCI86841; pmid: 27548528
80. X. Massana-Muñoz *et al*., Inactivating the lipid kinase activity of PI3KC2β is sufficient to rescue myotubular myopathy in mice. *JCI Insight* **8**, e151933 (2023). doi: 10.1172/jci.insight.151933; pmid: 36943412
81. D. G. Nowak *et al*., The PHLPP2 phosphatase is a druggable driver of prostate cancer progression. *J. Cell Biol.* **218**, 1943–1957 (2019). doi: 10.1083/jcb.201902048; pmid: 31092557
82. Z. T. Pennington *et al*., ezTrack: An open-source video analysis pipeline for the investigation of animal behavior. *Sci. Rep.* **9**, 19979 (2019). doi: 10.1038/s41598-019-56408-9; pmid: 31882950
83. C. Stringer, T. Wang, M. Michaelos, M. Pachitariu, Cellpose: A generalist algorithm for cellular segmentation. *Nat. Methods* **18**, 100–106 (2021). doi: 10.1038/s41592-020-01018-x; pmid: 33318659

ACKNOWLEDGMENTS

We acknowledge all the members of the Trotman laboratory, X. Jiang, V. Haucke, S. Gillessen-Sommer, A. Chabes, C. Tonelli, T. Oni, K. On, T. Miller, and S. Coutts for valuable advice and critical discussion of the data and manuscript. We thank G. DeNicola, V. Sanghvi, N. Tonks, M. Yamamoto, and W. X. Zong for reagents; P. Moody and C. Viola for help with FACS procedures; the Cold Spring Harbor Laboratory Animal Resources team, R. Rubino,

L. Bianco, J. Coblentz, and M. Cahn for help with animal work; A. Brady and J. Cheong for supplying validated cancer cell lines from CSHL's tissue culture facility; and D. Tsang for help with the article. We thank Q. Gao, A. Nourjanova, D. Hoppe-Cahn, K. Milicich, L. Stecher, and K. Anne-Javier for help with histologic procedures and analysis. We thank J. Kuhl for the mouse anatomy artwork. **Funding:** This work was directly supported by grants from the National Cancer Institute (NCI), 1R01CA275128 (L.C.T.) and NCI 5R01CA137050 (L.C.T.); the Pershing Square Sohn Cancer Research Alliance (L.C.T.); funds from IC-MedTech (L.C.T.); the Department of Defense grant DoD W81XWH-22-10-358 (M.R.D.); the Simons Foundation, Life Sciences Founders Directed Giving-Research award no. 519054 (M.W.); a research collaboration grant between AstraZeneca UK Limited and the Medical Research Council, reference BSF2-10 (R.L.W.); and the Mark Foundation for Cancer Research 20-028-EDV (T.J.) and NCI R01CA193256 (J.W.L.). D.A.T. is a distinguished scholar and Director of the Lustgarten Foundation–designated Laboratory of Pancreatic Cancer Research, supported by the Thompson Foundation, the Pershing Square Foundation, the Cold Spring Harbor Laboratory and Northwell Health Affiliation, the Northwell Health Tissue Donation Program, the Cold Spring Harbor Laboratory Association, and the National Institutes of Health (5P30CA45508, U01CA210240, R01CA229699, U01CA224013, 1R01CA188134, and 1R01CA190092). This research was furthermore supported by the Robertson Research Fund of Cold Spring Harbor Laboratory (L.C.T.), and it was done in collaboration with the Cold Spring Harbor Laboratory shared resources, which are supported by the National Institutes of Health (Cancer Center Support grant 5P30CA045508, D.A.T.) to support the flow cytometry, microscopy, functional genomics, tissue culture, MS, genome sequencing, gene targeting, animal husbandry, and histology analysis of this project. **Author contributions:** Conceptualization: M.M.S. and L.C.T. Experiments and data analysis: M.M.S., S.K., K.E.W., M.R.D., C.G., G.M., H.C., E.C., D.R., J.K., C.R.R., X.Z., T.H., S.K., O.K., J.Li., D.G.N., H.A., T.-L.W., Y.P., F.M., K.R., A.S.A., K.C., J.E.W., P.A.G., and S.D.D. SNS experiments: H.C., D.G.N., L.C.T., and J.K.; with help from A.S.A. and M.E.; under supervision of J.B.H., M.W., and L.C.T.; and analysis by M.M.S. and L.C.T., with help from J.K. RapidCaP animal generation and experiment execution: M.M.S., K.E.W., E.C., and T.H., with supervision and analysis by M.M.S., D.A.T., and L.C.T. CRISPR-Cas9 screens, concept, and execution: M.M.S., with help from K.C. and C.R.V., and data analysis by M.M.S. and L.C.T. MS and VPS34 biochemistry: J.Li., F.M., G.Q.G., R.P.C., S.Š., and A.N.D., supervised and analyzed by J.W.L., N.S.C., D.J.P., P.C., G.Q.G., R.L.W., M.M.S., and L.C.T. Myopathy analysis: C.G., D.R., and M.M.S., under supervision of T.J., L.C.T., and J.La. Data visualization: M.M.S. and L.C.T. Manuscript writing: G.Q.G., R.L.W., D.A.T., J.La., M.M.S., and L.C.T. **Competing interests:** R.L.W. received research funding from a grant involving AstraZeneca UK Limited. Unrelated to this work, M.E. has stock options in Agios Pharmaceuticals and was on the advisory board of Vividion Therapeutics. D.G.N. has patent WO2008110777 issued (Modulators of vegf splicing as pro- and antiangiogenic agents) with royalties paid and owns stock in Arvinas, Inc. D.A.T. receives stock options from Leap Therapeutics, Cygnal Therapeutics, Mestag Therapeutics, Xilis, and Dunad, all unrelated to the project. Also unrelated to this project, D.A.T. is a member of the scientific advisory boards for Leap Therapeutics, Cygnal Therapeutics, Mestag Therapeutics, Xilis, and Dunad; a scientific cofounder of Mestag Therapeutics; and has received research grant support from Fibrogen, Mestag, and ONO Therapeutics and has received consulting income from Amgen, all unrelated to this work. S.D.D. is founder and CSO of Amaroq Therapeutics Ltd. and RNAfold.AI Pty Ltd., T.J. consults for Flagship pioneering and LeapTx, and L.C.T. consults for Health Advances LLC, all unrelated to this work. **Data and materials availability:** All data are available in the manuscript and/or the supplementary materials.

SUPPLEMENTARY MATERIALS

Submitted 20 September 2023; accepted 27 August 2024
10.1126/science.adk9167